Anatomically distributed neural representations of instincts in the hypothalamus

Stefanos Stagkourakis[1, *], Giada Spigolon[2], Markus Marks[3], Michael Feyder[4], Joseph Kim[1], Pietro Perona[3], Marius Pachitariu[5, #], David J. Anderson[1, 6, #, *]

[1] Division of Biology and Biological Engineering 156-29, Tianqiao and Chrissy Chen Institute for Neuroscience, California Institute of Technology, Pasadena, California 91125, USA

[2] Biological Imaging Facility, California Institute of Technology, Pasadena, California 91125, USA

[3] Division of Engineering and Applied Science, California Institute of Technology, Pasadena, California 91125, USA

[4] Division of Psychiatry and Behavioral Sciences, Stanford University, Palo Alto, California 94305, USA

[5] Howard Hughes Medical Institute, Janelia Research Campus, Ashburn, VA, USA

[6] Howard Hughes Medical Institute, California Institute of Technology, 1200 East California Blvd, Pasadena, California 91125, USA

[#] Joint supervision

* Correspondence:

stefanos.stagkourakis@gmail.com (S.S.),

wuwei@caltech.edu (D.J.A.)

Summary

Artificial activation of anatomically localized, genetically defined hypothalamic neuron populations is known to trigger distinct innate behaviors, suggesting a hypothalamic nucleus-centered organization of behavior control. To assess whether the encoding of behavior is similarly anatomically confined, we performed simultaneous neuron recordings across twenty hypothalamic regions in freely moving animals. Here we show that distinct but anatomically distributed neuron ensembles encode the social and fear behavior classes, primarily through mixed selectivity. While behavior class-encoding ensembles were spatially distributed, individual ensembles exhibited strong localization bias. Encoding models identified that behavior actions, but not motion-related variables, explained a large fraction of hypothalamic neuron activity variance. These results identify unexpected complexity in the hypothalamic encoding of instincts and provide a foundation for understanding the role of distributed neural representations in the expression of behaviors driven by hardwired circuits.

Introduction

Brains evolved to create a series of abstractions that represent objects or other sensory cues in an organism's environment, assess their value, predict impending changes in their features, and transform those signals into adaptive behavioral responses. To deconstruct this complex process, two main experimental strategies have been taken to either: 1) record neural activity during behavior, or 2) manipulate neural activity and observe changes in behavior. The first strategy starts with measurements of neuronal activity and correlates those data with manipulations and measurements of sensory features or task variables[1-5]. The behavioral readouts typically involve artificial tasks that require intensive training and are highly reproducible across trials. In mammals, this strategy has been employed to study the cortex, hippocampus, or other evolutionarily recent areas[6-10], and their influence on cognitive functions.

The second strategy starts with surgical, electrical, neurochemical, or genetically-based perturbation experiments to identify brain regions and cell types whose activation, inhibition, or destruction can promote or suppress particular behaviors. These manipulations are targeted to pre-selected areas based on hypotheses, assumptions, or prior knowledge. This strategy has dominated the study of internal states, motivation, reward, and emotion[11-15]. The behavioral readouts typically comprise innate behaviors or simple forms of conditioning based on such instincts. The study of such functions has typically focused on the so-called "limbic system," including evolutionarily ancient regions such as the extended amygdala[16,17], hypothalamus[18,19], and midbrain[20,21].

The two above-mentioned strategies can yield fundamentally different views of the mechanisms underlying brain functions of interest. Although many studies in practice employ both strategies sequentially, prevailing views in a field are often strongly shaped by the approach that was initially undertaken[22-24]. The "recording first" strategy has led to an emphasis on high-dimensional population codes, neural dynamics, and manifolds in cortico-hippocampal state space. Nevertheless, the field is increasingly employing perturbation experiments to test hypotheses based on observational studies. In contrast, the "perturbation first" strategy has led to an emphasis in the hypothalamus field on hard-wired

neural circuits that causally control specific innate behaviors in a manner that is highly deterministic and low-dimensional[25-27]. However, large-scale recording experiments in this field have been relatively rare.

It remains unclear, therefore, whether these different views of how cortical and limbic systems control behavior reflect true biological differences, or rather differences in the evolution of these fields according to the initial experimental strategies used at their inception. To help resolve this discrepancy, here we have performed large-scale recordings from neural populations located along the rostrocaudal axis of the medial hypothalamus, using custom-designed silicon probes in freely moving mice engaged in solitary, social, or predator-defense behaviors. Our results reveal that the neural coding of such instinctive behaviors is, surprisingly, more distributed, dynamic, and high-dimensional than would have been expected from perturbation experiments. These results invite a re-evaluation of views of neural coding principles in cortical vs. limbic areas and highlight the importance of integrating results from observational and perturbational studies to arrive at a comprehensive understanding of brain function.

Results

Recording single neurons across multiple sites of the hypothalamus during behavior

We sought to acquire synchronized large-scale electrophysiological and video recording data from freely moving mice engaging in diverse innate behaviors. To record the activity of hundreds of neurons simultaneously throughout the medial hypothalamus, we used a custom-fabricated silicon probe (NeuroNexus, Inc.) that allows chronic extracellular electrophysiological recordings (with single-unit resolution) from multiple nuclei (Figure 1A). The eight-shank 256-channel silicon probe (Figure 1B) was designed to provide simultaneous access to twenty hypothalamic subregions (nuclei or subnuclei), which are spatially distributed across the rostrocaudal extent of the hypothalamus (Figure 1E). The probe covers ~2.3mm of brain tissue (Figure 1A, lower), and we recorded ~400 units per animal (n=6 animals) for a total of 2,347 units.

To map shank trajectories, the back side of the probe shanks was coated with a red lipophilic dye that could be traced post-hoc. Intact iDISCO-cleared mouse brains were volumetrically imaged using light-sheet microscopy[28], and probe coordinates were mapped to the Allen Common Coordinate Framework[29] (Figure 1C and 1D). A unique electrode map was generated for each mouse by manually mapping electrodes to computationally sectioned sagittal sections of each mouse brain (Figures S1A-S1B). A schematic map of the areas recorded in each mouse is shown in Figure 1E. Based on the electrode maps, neurons were allocated to specific hypothalamic brain areas (Figure 1F, single-neuron activity colored according to the location of each neuron). Spike-sorting was performed using Kilosort[30], and basic analysis of neuron waveforms (Figure 1G), and quality control of recordings was performed using pre-existing pipelines (see also STAR Methods section: *in vivo* electrophysiology). Neural data were analyzed in relation to behavior either a) with single neuron resolution (Figure 1H – upper part), or b) by averaging the activity of cells per nucleus (Figure 1H – lower part). This experimental design enabled us to test whether the encoding of behavior in the hypothalamus conforms to anatomical nuclear

97 boundaries and examine the extent to which neurons from the same nucleus are highly correlated or
98 have distinct activity patterns across diverse behaviors. (Figure 1I).

99 To investigate the representation of behavior in the hypothalamus, we grouped behaviors into three
100 hierarchical levels (Figure 1I, right). At the highest level, we defined three broad behavioral categories
101 which we refer to as "classes": the solitary class includes actions such as self-grooming, and rearing. The
102 social class includes behaviors such as sniffing a male or female conspecific or attacking a male
103 conspecific. The fear class includes behaviors such as sniffing a predator or exhibiting an escape
104 response. At the second level, we distinguished two "domains" within the "social" class: intermale and
105 male-female social behaviors (Figure 1I, right; green and violet, respectively). Finally, at the third and
106 lowest level, we annotated 43 distinct actions among the different classes and domains (Figure 3B).

107 To ensure that the behaviors of interest would be expressed during the neural data recording
108 sessions, animals (male Swiss-Webster mice) were pre-screened for robust performance in the relevant
109 behavioral assays (Figure 2A, a) solitary, b) social, and c) fear). This pre-screening step reinforced the
110 expression of social behaviors[11,12], and the display of fear behaviors during the recording sessions (Figure
111 S1C-S1I). Following the probe implantation, animals were allowed to recover and were habituated to the
112 experimental setup in the absence of the behavioral assays (Figure 2B).

113 As previous work has shown that neural firing rates often correlate with motion-related variables in
114 some brain areas[31-33], we assessed this question in our mesoscale hypothalamic recordings. Self-motion
115 variables and distance between animals did not correlate with mean single unit firing rates, either during
116 whole recording sessions (Figures S2A and S2Ba-S2Bc), or during specific behavior actions (Figure
117 S2Bd). Partial least squares (PLS) regression provided further evidence that single-unit activity also does
118 not correlate with motion variables (Figure S2C, note a near zero R^2 between PLS components of neural
119 data and of motion-related variables in Figure S2Cd). However, the PLS regression revealed that single-
120 unit activity was correlated with consummatory (Figure S2D, note a high R^2 between PLS components
121 of neural data and of consummatory behaviors in Figure S2Dd), and, to a lesser extent, with appetitive

(Figure S2E, note a medium range R^2 between PLS components of neural data and of appetitive behaviors in Figure S2Ed) social and fear behaviors.

Spatially distributed and behavior non-specific neural "ignition signals"

Next, we sought to address whether activity during specific appetitive and consummatory behaviors, including intermale social behaviors (Figure 2C and 2D), male-female social behaviors (Figure 2E and 2F), and predatory defensive behaviors (Figure 2G and 2H), is restricted anatomically or rather spatially distributed, based on averaging units recorded from each of the twenty nuclei. Throughout the entire hypothalamus, we observed a synchronous burst of activity near the onset of all behaviors except for predator-induced freezing (Figure 2C-2G). This spiking burst that occurred at all behavior onsets following the introduction of an intruder, appeared consistently across behavioral episodes (Figure S2F and S2G). It had an onset of -200 msec prior to the initiation of behavior (Figure S2H and S2Ia), an average duration of 1.5 sec (Figure S2Ib), and always ended before the termination of the behavior (Figure S2Ic). This response, which we refer to here as an "ignition signal," encompassed ~25-35% of recorded units across the entire hypothalamus, except for freezing behavior which engaged only 7% of units (Figure 2D-H, gray/black pie charts). The ignition signal was observed across multiple episodes of a given behavior directed towards the same intruder or predator (Figure S2F), indicating that it did not simply represent a novelty or neophobic response. However, the activity levels and proportion of the neurons recruited across behaviors markedly differed across nuclei (Figure 2C, 2E, and 2G – right bar plots). Each nucleus was differentially activated during behaviors of interest (Figure 2D, 2F, and 2H). Together, these findings indicate that ignition signals, while globally distributed, exhibit quantitative biases in their anatomic distribution that likely reflect behavior-specific responses in different hypothalamic nuclei (Figure 2D, 2F, and 2H).

The near-uniform expression of ignition signals likely accounts for the lack of statistical significance in decoding behaviors from nucleus-averaged neural activity (SVM decoding models, Figure S2J). An

147 analysis of activity at single-unit resolution – discussed in the next section, however, could help to address
148 whether behavior-specific modes of activity exist at the level of individual neurons.
149

150 **Single neuron activity primarily encodes distinct behavior classes**

151 To investigate the representation of behavior by single neurons in the hypothalamus, we annotated
152 43 behavioral actions among the different classes and domains (functional models discussed in Figure
153 1I, right). Using these annotations, the first approach we used was to compute the single neuron activity-
154 based behavior correlation matrix (Figure 3Aa-3Ad). Using rastermap[34], we sorted the row and column
155 indices of the behavior correlation matrix to maximize similarity between consecutive rows and columns,
156 which allowed us to evaluate the differences in neural representations across behaviors visually (Figure
157 3B). Following averaging of the behavior correlation matrix across six mice, we observed a prominent
158 segregation between social and predatory-defensive behavioral classes (note the separation of red-
159 ["fear"] vs. green- and purple-tagged [social] behaviors in Figure 3B). This effect was also prominent in
160 the behavior correlation matrices of individual mice (Figure S3Aa-S3Af, with the notable exception of
161 mouse #4, whose behavior correlation matrix is shown in Figure S3Ad). Overall, this analysis revealed
162 that social and fear behavioral classes can be broadly segregated based on neuron population activity.
163 Male- and female-directed social behaviors were also generally separated, but not as prominently.
164 Related individual actions had correlated neural patterns to some extent within domains (Figure 3B,
165 sorting of behavior actions reflects similarity in their encoding).

166 The results of the behavior correlation matrix suggested that social and fear behaviors are encoded
167 differently by hypothalamic neurons. However, this population-level analysis cannot distinguish whether
168 individual behaviors are encoded by the same set of neurons that exhibit behavior class-specific activity
169 patterns or whether distinct groups of neurons encode distinct behavior classes. To address this question,
170 we next used a more targeted method, focusing on only two representative behavioral actions from each
171 of the four behavioral domains of interest (a total of eight behavioral actions, Figure 4A). This approach
172 could 1) confirm or disprove the segregation of social vs. fear behaviors, and 2) if the former is the case,

173 indicate whether this segregation reflects different neuron groups active in the two behavioral classes, or
174 whether it is driven by different patterns of activity exhibited by the same neurons.

175 In the solitary domain, the self-grooming (sg) and rearing (r) behavioral actions were included.
176 Representative behavioral actions in the intermale domain were male intruder sniffing (ms), and attack
177 (ma), while in the male-female domain female intruder sniffing (fs) and mounting (fm) were included.
178 Lastly, in the predatory fear domain, the rat sniffing (rs) and escape response (re) behavior actions were
179 included. The time points of three episodes per behavior were extracted from the experimental design
180 illustrated in Figure 3Aa. Specifically, solitary behavior episodes were extracted from experiment (a),
181 female-oriented behavior episodes were extracted from experiments (a) and (b), male-oriented behavior
182 episodes were extracted from experiments (c) and (d), and predator-defence behavior episodes were
183 extracted from experiment (e). Figure S4A shows the activity of single units across the eight above-
184 mentioned behavioral actions, across three consecutive behavioral episodes. The activity of single units
185 was sorted from high to low within each brain area.

186 To test whether separate groups of recorded units exhibit distinct behavior-correlated activity profiles,
187 we performed *k*-means clustering of the single neuron activity (Figure S4A). The number of clusters, 41,
188 was selected using the elbow method[35,36]; 41 clusters explained 70% of the single neuron activity data
189 variance. The average activity of each of the 41 clusters during the 8 different domain-specific actions
190 was plotted for each of the three consecutive episodes (Figure 4A). Agglomerative hierarchical linkage
191 clustering (ALC) of these 41 clusters revealed five groups (i.e., dendrogram branches, Figure 4A, right,
192 threshold for separating branches of the dendrogram was defined using the elbow method). This analysis
193 suggested that the social and fear behavior classes are encoded by functionally distinct groups of
194 hypothalamic neurons (Figure 4A, highlighted as blue [social] and red [predatory fear] clusters in the
195 dendrogram). This finding was also qualitatively supported by performing non-negative matrix
196 factorization (NMF) on the data shown in Figure S4A. However, with NMF, the distinction between social-
197 vs. fear-correlated ensemble activity was less prominent (Figure S5A and S5B). The weaker segregation

198 of behavioral classes through NMF likely reflects that NMF allows neurons to contribute to multiple factors
199 (components).

200 While the *k*-means clusters associated with social or fear behavior classes were well separated,
201 neurons exhibited multi-action activity, also known as mixed selectivity, within each class-specific cluster
202 (Figure 4B). To quantify this finding, we classified a cluster as active during a specific action if its activity
203 (spiking rate) was $\geq 2\sigma$ above its baseline activity. Accordingly, 56% of all clusters were identified to
204 exhibit mixed selectivity within their respective behavior classes. Only seven percent of hypothalamic
205 clusters exhibited mixed selectivity within a single behavioral domain (male- or female-directed behavior;
206 Figure 4C), while 27% of clusters showed prominent activity during only a single action (Figure 4D). While
207 the activity of any single cluster exhibited adaptation across episodes (Figure S4B) there was an overall
208 positive correlation between episodes (Figure S4C) and a high-fidelity score (a measure of a cluster being
209 identified as active in the same behavior(s) across episodes, Figure S4D). Thus, the representation of
210 behavioral actions by different clusters is reproducible across episodes, but not rigidly fixed.

211

212 **Encoding of behavior is spatially distributed, but individual ensembles are**
213 **anatomically localized**

214 The foregoing analysis revealed that distinct neuron clusters encode social and fear behavior classes.
215 We next sought to determine whether individual activity-defined ensembles are anatomically localized
216 and whether they respect classical cytoarchitectonically defined nuclear boundaries.

217 We found that a) functionally similar clusters were distributed broadly across the hypothalamic
218 rostrocaudal axis (Figure 5A), and b) that most clusters were composed of cells that originated from a
219 few neighboring hypothalamic regions (Figure 5B). Re-sorting these clusters within each branch of the
220 dendrogram according to their position along the rostro-caudal axis (Figure 5C), revealed that each
221 behavior class was broadly represented along this axis (Figure 5C).

222 The number of regions contributing to single clusters was typically four areas (Figure 5D), suggesting
223 that most hypothalamic clusters consist of cells that originate from four neighboring hypothalamic regions.
224 The same observation occurred when quantifying the composition of clusters that were identified as
225 "social", female-specific, and predatory-fear relevant (Figure 5D – inset). We investigated whether
226 increasing the number of clusters in *k*-means leads to a reduced number of regions per cluster (Figure
227 5E). However, we found an asymptote at an average number of four nuclei per cluster which did not
228 further decrease even when the number of clusters was increased up to 120 (Figure 5E). The smallest
229 number of clusters that reached the asymptotic value of 4 regions per cluster was 41, and this model
230 explained a majority of the variance in the data (70%). A qualitatively similar result emerged when
231 analyzing factors identified by NMF, with closely related factors composed of neurons at different
232 positions along the rostrocaudal axis, and heavily weighted neurons in each factor were present in
233 neighboring hypothalamic regions (Figure S5C-S5E).
234

235 **Behavior explains a quarter of the variance of hypothalamic neuron activity**

236 The above approaches suggest that: 1) distinct populations of neurons represent social and fear
237 behaviors, 2) the encoding of each behavioral class is represented by a set of clusters comprised of units
238 defined by correlated neuronal activity, which are spatially distributed across the rostro-caudal axis, and
239 3) individual clusters typically contained neurons from ca. four neighboring nuclei, therefore exhibiting a
240 strong local anatomical bias in their composition. However, since most of the units in these functional
241 clusters exhibited mixed selectivity, it remained uncertain whether specific behavior actions could be
242 decoded from neural activity.

243 To determine whether individual behavioral actions could be predicted from single-unit activity, we
244 trained decoders based on neural activity using two different machine learning algorithms (gradient
245 boosted trees [37], results plotted in Figure S6A and S6B, and support vector machines [23], results plotted
246 in Figure S6C-S6E). A subset of appetitive and consummatory representative behavior actions per

behavioral domain were selected to address the above point. The results indicated that most, but not all, actions within each of the four different behavioral domains could be decoded from neural data significantly better than chance. In the case of male-directed attack, decoder performance was high, reaching a shuffled subtracted median F1 score of ~0.5 (Figure S6B).

The foregoing analysis suggested that behavioral actions could be decoded from neural activity but left open the question of which features of these behaviors were encoded. To address this question, we next examined how well the firing patterns of individual units could be predicted from a weighted sum of different behavioral actions and features (features included animal's velocity, acceleration, distance, and angle between animals). These features were computed based on pose estimation using DeepLabCut [38]. We trained generalized linear models (GLMs) [39,40] to predict the activity of each neuron based on a weighted sum of selected predictor variables (design of GLMs shown in Figure 6A). This approach can: 1) identify the overall variance explained by specific predictors (Figure 6B), 2) reveal the influence of all annotated predictors on single neuron activity, by inspection of their coefficients/weights (Figure 6C), and 3) indicate whether neurons that belong to the same cluster (based on the similarity of their behavior weights – Figure 6C, see dendrogram colored branches) show any spatial bias (Figure 6D and 6E).

First, we sought to identify the percentage of variance explained by the four high-level behavior classes. Only 8% of the variance of single-neuron activity was accounted for by the four behavioral domains (Figure S6Fa). Next, we examined the percent of variance explained by forty behavioral actions, annotated across the four behavioral domains of interest. Behavioral actions alone explained 23% of the variance of hypothalamic neuron activity (R^2 median = 0.23, Figure 6B). Training GLM models with predictor variables being the behavioral actions, plus motion signals (the animals' velocity and acceleration), and proxies of sensory cues (distance and angle between animals), did not lead to an increase in the variance explained (Figure S6Ga and S6Gb).

Many different behaviors had positive and negative weights on the activity pattern of each single unit (Figure 6C), highlighting mixed selectivity as a prime mode of the hypothalamic encoding of behavior, and providing further support to the results of the *k*-means (Figure 4B) and NMF analysis (Figure S5A).

Application of agglomerative clustering (ALC) to the matrix of GLM-derived behavior weights yielded 24 clusters of neurons (the elbow method was used to select the number of clusters). Each cluster (Figure 6C) contained a unique combination of neurons whose activity was influenced by a specific set of behavior weights (Figure 6C), with a near-uniform contribution of neurons from each of the six recorded mice (Figure S6H). Sorting these neurons based on their relative spatial location, however, did not generate clusters in a pattern similar to that identified by ALC, suggesting that the neurons comprising the clusters are not restricted to single hypothalamic nuclei (Figure S6I). To investigate whether the cells comprising the ALC-generated neuron clusters exhibit any restriction in their anatomic distribution, we measured the average contribution of each nucleus to each cluster (Figure 6D, rows). This revealed that clusters indeed exhibited a spatial bias, with >80% of the cells comprising each cluster originating from ~four nearby regions (Figure 6D and 6E) – a finding consistent with the *k*-means-revealed cluster anatomical bias (Figure 5B). Also similar to the *k*-means analysis, we found that GLM-based clusters exhibited spatial bias and mixed selectivity (Figure 6F), quantified using a spatial localization index (single nucleus restricted vs. broadly distributed) and encoding entropy respectively (the degree of behavior specific vs. mixed selectivity coding; see STAR Methods section: GLM output – functional vs. spatial distribution of clusters).

Discussion

The hypothalamus is traditionally viewed as a "low-dimensional" system in which innate social, defensive, and feeding behaviors are controlled by bulk neural activity flowing through specific pathways connecting functionally specialized anatomical subdivisions and cell types[41-43]. In contrast, the cortico-hippocampal system is thought to operate using high-dimensional, dynamic neural codes involving complex spatiotemporal patterns of population activity[44-47]. Here, we addressed whether this difference is truly biological or reflects the fact that most recording studies in the hypothalamus have used low-dimensional recording methods (e.g., fiber photometry) applied to anatomically restricted regions pre-selected based on perturbational studies. We report here what is, to our knowledge, the first unbiased high-dimensional single-unit recording of neural activity along the rostrocaudal axis of the medial hypothalamus during social and predator-defense behaviors. Our results suggest that behavioral coding in the hypothalamus is more high-dimensional, spatially distributed, dynamic, and variable than previously appreciated.

Several unexpected findings have emerged from this study. First, we observe that the initiation of these innate behaviors is (except for freezing) preceded by a hypothalamus-wide, synchronous burst of peri-onset activity, which we call an "ignition signal." Second, we find that functionally distinct subpopulations of neurons (defined by unbiased *k*-means clustering) encode social (mating and fighting) vs. predator defense behavioral classes. Specific behavioral actions or male- vs. female-directed social behaviors are less well-discriminated by such clusters. While these clusters are reproducibly activated across multiple episodes of each behavioral class, inter-episodic variability exists in the recruitment and activity level of the neurons comprising each cluster. Nevertheless, despite this variability, many behavioral actions could be decoded from single-unit activity with high accuracy. Third, we find that the subpopulations representing social and defense behaviors are broadly distributed across the rostrocaudal length of the hypothalamus rather than spatially localized to a single nucleus or region. Fourth, we find that cluster membership draws from neurons distributed in neighboring nuclei, typically

314 four. Nevertheless, behavior cannot be decoded from bulk neural activity based on anatomical location
315 alone. Finally, we find that a substantial fraction (median 23%) of the single-neuron variance in activity
316 can be explained by behavioral actions and, to a lesser degree, by behavioral domains. We consider the
317 median R^2 of 0.23 as a high value, as other studies which used brain-wide recordings during stereotyped
318 behavioral tasks in head-fixed mice reported a cross-validated variance explained in single neuron
319 activity in the range of 5-15%[48,49].

320 The present study paints an overall picture that challenges prevailing views of behavioral encoding
321 by the hypothalamus. We note that if these data had provided the very first, foundational view of
322 hypothalamic behavioral encoding, they would not have directed subsequent functional perturbations to
323 specific single nuclei such as VMH[11,13,22,23,50-55] or MPOA[14,56-60]. Instead, they would have prompted the
324 study of behavior encoding units across several neighboring nuclei. They would have shifted the focus
325 from seeking the identification of behavior-specific cell types to understanding the properties conferred
326 by the prime mode of activity we report here, i.e., mixed selectivity[61-65].

327 Is there any way to reconcile these two seemingly opposing views of behavioral control by the
328 hypothalamus? There are several possible explanations. One possibility is that prior, low-dimensional,
329 anatomically restricted approaches have missed what is suggested by our silicon probe recordings: i.e.,
330 that the "units" of hypothalamic computations are anatomically distributed, and that mixed-selectivity is
331 the prime mode of hypothalamic behavioral encoding. Recent studies suggest that even in the absence
332 of behavior action-tuned cells, behavior can still be decoded with high accuracy, with mixed selectivity
333 providing a basis for the encoding of numerous and diverse features in a computationally efficient manner
334 [61-64]. For example, nonlinear mixed selectivity enables the integration of diverse lines of information in
335 single neurons that can elicit behavior actions based on a threshold mechanism.

336 A second possibility is that our silicon probe recordings have missed anatomically restricted behavior-
337 specific subsets. This could be due to sparse sampling (we recorded on average only ~20 units per
338 nucleus per animal) and/or to variability in the activity of individual units across episodes and animals

during a given behavior, perhaps reflecting representational drift[66,67] or stochastic recruitment of individual units[68]. This variability may explain, in part, why a recent multi-site coarse recording of bulk calcium activity from Esr1$^+$ neurons across the hypothalamus yielded reproducible, spatially distinct patterns of activity during male- vs. female-directed social behaviors, in specific nuclei previously identified as causally relevant to these behaviors by perturbation studies[69]. Alternatively, Esr1$^+$ neurons may represent a "privileged," more behavior-specific subpopulation than the "anonymous" units sampled here. A third possibility (not mutually exclusive with the second) is that the intrinsic variability in the performance or sequence of specific behavioral actions during a given activity (e.g., a male-male social interaction) may confound efforts to correlate a high-granularity annotation of these actions (43) with high-dimensional neural data (~2400 units from 6 animals). Finally, we note that causation and representation are not the same thing: not all neural representations during a given behavior necessarily reflect a causal role for those neurons; for example, some activated units may represent efference copies of motor signals, or GABAergic neurons that serve to inhibit competing behaviors.

Further work is required to distinguish these possibilities and to arrive at an understanding of behavioral coding and function that reconciles and integrates the two views of hypothalamic computations provided by recording and perturbation strategies, respectively. At the very least, our data indicate that the application to the hypothalamus of unbiased, large-scale, anonymous single-unit recordings reveals a surprisingly complex pattern of spatiotemporal activity that does not easily map to specific nuclei or single behavior actions. It suggests that the prevailing view of the hypothalamus as a low-dimensional control system needs to be revised, or alternatively that the signals that control behavior are, to a large extent, "hidden" in the population code.

References

1. Lin, X.D., Wang, S.Q., Yu, X.D., Liu, Z.G., Wang, F., Li, W.T., Cheng, S.H., Dai, Q.Y., and Shi, P. (2015). High-throughput mapping of brain-wide activity in awake and drug-responsive vertebrates. Lab on a chip *15*, 680-689. 10.1039/c4lc01186d.
2. Litvina, E., Adams, A., Barth, A., Bruchez, M., Carson, J., Chung, J.E., Dupre, K.B., Frank, L.M., Gates, K.M., Harris, K.M., et al. (2019). BRAIN Initiative: Cutting-Edge Tools and Resources for the Community. Journal of Neuroscience *39*, 8275-8284. 10.1523/Jneurosci.1169-19.2019.
3. Perich, M.G., and Rajan, K. (2020). Rethinking brain-wide interactions through multi-region 'network of networks' models. Current opinion in neurobiology *65*, 146-151. 10.1016/j.conb.2020.11.003.
4. Edelman, B.J., and Macé, E. (2021). Functional ultrasound brain imaging: Bridging networks, neurons, and behavior. Current Opinion in Biomedical Engineering *18*. 10.1016/j.cobme.2021.100286.
5. Schrodel, T., Prevedel, R., Aumayr, K., Zimmer, M., and Vaziri, A. (2013). Brain-wide 3D imaging of neuronal activity in Caenorhabditis elegans with sculpted light. Nature methods *10*, 1013-1020. 10.1038/nmeth.2637.
6. Brodt, S., Gais, S., Beck, J., Erb, M., Scheffler, K., and Schönauer, M. (2018). Fast track to the neocortex: A memory engram in the posterior parietal cortex. Science *362*, 1045-+. 10.1126/science.aau2528.
7. Chersi, F., and Burgess, N. (2015). The Cognitive Architecture of Spatial Navigation: Hippocampal and Striatal Contributions. Neuron *88*, 64-77. 10.1016/j.neuron.2015.09.021.
8. Doeller, C.F., Barry, C., and Burgess, N. (2010). Evidence for grid cells in a human memory network. Nature *463*, 657-U687. 10.1038/nature08704.
9. Grieco, S.F., Holmes, T.C., and Xu, X.M. (2023). Probing neural circuit mechanisms in Alzheimer's disease using novel technologies. Mol Psychiatr. 10.1038/s41380-023-02018-x.
10. Tomé, D.F., Sadeh, S., and Clopath, C. (2022). Coordinated hippocampal-thalamic-cortical communication crucial for engram dynamics underneath systems consolidation. Nature communications *13*. 10.1038/s41467-022-28339-z.
11. Stagkourakis, S., Spigolon, G., Liu, G., and Anderson, D.J. (2020). Experience-dependent plasticity in an innate social behavior is mediated by hypothalamic LTP. Proceedings of the National Academy of Sciences of the United States of America *117*, 25789-25799. 10.1073/pnas.2011782117.
12. Stagkourakis, S., Spigolon, G., Williams, P., Protzmann, J., Fisone, G., and Broberger, C. (2018). A neural network for intermale aggression to establish social hierarchy. Nature neuroscience *21*, 834-+. 10.1038/s41593-018-0153-x.
13. Lin, D., Boyle, M.P., Dollar, P., Lee, H., Lein, E.S., Perona, P., and Anderson, D.J. (2011). Functional identification of an aggression locus in the mouse hypothalamus. Nature *470*, 221-226. 10.1038/nature09736.
14. Karigo, T., Kennedy, A., Yang, B., Liu, M.Y., Tai, D., Wahle, I.A., and Anderson, D.J. (2021). Distinct hypothalamic control of same- and opposite-sex mounting behaviour in mice (vol 589, pg 258, 2021). Nature *589*, E9-E9. 10.1038/s41586-020-03143-1.
15. Kunwar, P.S., Zelikowsky, M., Remedios, R., Cai, H.J., Yilmaz, M., Meister, M., and Anderson, D.J. (2015). Ventromedial hypothalamic neurons control a defensive emotion state. eLife *4*. 10.7554/eLife.06633.
16. Adhikari, A., Lerner, T.N., Finkelstein, J., Pak, S., Jennings, J.H., Davidson, T.J., Ferenczi, E., Gunaydin, L.A., Irzabekov, J.J.M., Ye, L., et al. (2015). Basomedial amygdala mediates top-down control of anxiety and fear. Nature *527*, 179-+. 10.1038/nature15698.
17. Kim, J., Zhang, X.Y., Muralidhar, S., LeBlanc, S.A., and Tonegawa, S. (2017). Basolateral to Central Amygdala Neural Circuits for Appetitive Behaviors. Neuron *93*, 1464-+. 10.1016/j.neuron.2017.02.034.
18. Scott, N., Prigge, M., Yizhar, O., and Kimchi, T. (2015). A sexually dimorphic hypothalamic circuit controls maternal care and oxytocin secretion. Nature *525*, 519-+. 10.1038/nature15378.

19. Stagkourakis, S., Spigolon, G., Liu, G., and Anderson, D.J. (2020). Experience-dependent plasticity in an innate social behavior is mediated by hypothalamic LTP. Proceedings of the National Academy of Sciences of the United States of America *117*, 25789-25799. 10.1073/pnas.2011782117.
20. Mahadevia, D., Saha, R., Manganaro, A., Chuhma, N., Ziolkowski-Blake, A., Morgan, A.A., Dumitriu, D., Rayport, S., and Ansorge, M.S. (2021). Dopamine promotes aggression in mice via ventral tegmental area to lateral septum projections. Nature communications *12*. 10.1038/s41467-021-27092-z.
21. Falkner, A.L., Wei, D., Song, A., Watsek, L.W., Chen, I., Chen, P., Feng, J.E., and Lin, D. (2020). Hierarchical Representations of Aggression in a Hypothalamic-Midbrain Circuit. Neuron *106*, 637-648 e636. 10.1016/j.neuron.2020.02.014.
22. Lee, H., Kim, D.W., Remedios, R., Anthony, T.E., Chang, A., Madisen, L., Zeng, H., and Anderson, D.J. (2014). Scalable control of mounting and attack by Esr1+ neurons in the ventromedial hypothalamus. Nature *509*, 627-632. 10.1038/nature13169.
23. Remedios, R., Kennedy, A., Zelikowsky, M., Grewe, B.F., Schnitzer, M.J., and Anderson, D.J. (2017). Social behaviour shapes hypothalamic neural ensemble representations of conspecific sex. Nature *550*, 388-+. 10.1038/nature23885.
24. Nair, A., Karigo, T., Yang, B., Ganguli, S., Schnitzer, M.J., Linderman, S.W., Anderson, D.J., and Kennedy, A. (2023). An approximate line attractor in the hypothalamus encodes an aggressive state. Cell *186*, 178-193 e115. 10.1016/j.cell.2022.11.027.
25. Asaba, A., Nomoto, K., Osakada, T., Matsuo, T., Kobayakawa, K., Kobayakawa, R., Touhara, K., Mogi, K., and Kikusui, T. (2022). Prelimbic cortex responds to male ultrasonic vocalizations in the presence of a male pheromone in female mice. Frontiers in neural circuits *16*. 10.3389/fncir.2022.956201.
26. Ishii, K.K., and Touhara, K. (2019). Neural circuits regulating sexual behaviors via the olfactory system in mice. Neuroscience research *140*, 59-76. 10.1016/j.neures.2018.10.009.
27. Itakura, T., Murata, K., Miyamichi, K., Ishii, K.K., Yoshihara, Y., and Touhara, K. (2022). A single vomeronasal receptor promotes intermale aggression through dedicated hypothalamic neurons. Neuron *110*, 2455-2469 e2458. 10.1016/j.neuron.2022.05.002.
28. Renier, N., Wu, Z.H., Simon, D.J., Yang, J., Ariel, P., and Tessier-Lavigne, M. (2014). iDISCO: A Simple, RapidMethod to Immunolabel Large Tissue Samples for Volume Imaging. Cell *159*, 896-910. 10.1016/j.cell.2014.10.010.
29. Wang, Q.X., Ding, S.L., Li, Y., Royall, J., Feng, D., Lesnar, P., Graddis, N., Naeemi, M., Facer, B., Ho, A., et al. (2020). The Allen Mouse Brain Common Coordinate Framework: A 3D Reference Atlas. Cell *181*, 936-+. 10.1016/j.cell.2020.04.007.
30. Steinmetz, N.A., Aydin, C., Lebedeva, A., Okun, M., Pachitariu, M., Bauza, M., Beau, M., Bhagat, J., Bohm, C., Broux, M., et al. (2021). Neuropixels 2.0: A miniaturized high-density probe for stable, long-term brain recordings. Science *372*, 258-+. 10.1126/science.abf4588.
31. Vinck, M., Batista-Brito, R., Knoblich, U., and Cardin, J.A. (2015). Arousal and Locomotion Make Distinct Contributions to Cortical Activity Patterns and Visual Encoding. Neuron *86*, 740-754. 10.1016/j.neuron.2015.03.028.
32. Dadarlat, M.C., and Stryker, M.P. (2017). Locomotion Enhances Neural Encoding of Visual Stimuli in Mouse V1. Journal of Neuroscience *37*, 3764-3775. 10.1523/Jneurosci.2728-16.2017.
33. Christensen, A.J., and Pillow, J.W. (2022). Reduced neural activity but improved coding in rodent higher-order visual cortex during locomotion. Nature communications *13*, 1676. 10.1038/s41467-022-29200-z.
34. Stringer C., Z.L., Syeda A., Du F., Kesa M., & Pachitariu M. (2023). Rastermap: a discovery method for neural population recordings. bioRxiv. https://doi.org/10.1101/2023.07.25.550571.
35. Goutte, C., Toft, P., Rostrup, E., Nielsen, F.Å., and Hansen, L.K. (1999). On clustering fMRI time series. NeuroImage *9*, 298-310. DOI 10.1006/nimg.1998.0391.
36. Thorndike, R.L. (1953). Who Belongs in the Family? Psychometrika *18*, 267-276.

37. Viejo, G., Cortier, T., and Peyrache, A. (2018). Brain-state invariant thalamo-cortical coordination revealed by nonlinear encoders. PLoS computational biology *14*. 10.1371/journal.pcbi.1006041.
38. Mathis, A., Mamidanna, P., Cury, K.M., Abe, T., Murthy, V.N., Mathis, M.W., and Bethge, M. (2018). DeepLabCut: markerless pose estimation of user-defined body parts with deep learning. Nature neuroscience *21*, 1281-1289. 10.1038/s41593-018-0209-y.
39. Weber, A.I., and Pillow, J.W. (2017). Capturing the Dynamical Repertoire of Single Neurons with Generalized Linear Models. Neural computation *29*, 3260-3289. 10.1162/neco_a_01021.
40. Park, I.M., Meister, M.L.R., Huk, A.C., and Pillow, J.W. (2014). Encoding and decoding in parietal cortex during sensorimotor decision-making. Nature neuroscience *17*, 1395-1403. 10.1038/nn.3800.
41. Mei, L., Osakada, T., and Lin, D. (2023). Hypothalamic control of innate social behaviors. Science *382*, 399-404. 10.1126/science.adh8489.
42. Hahn, J.D., Fink, G., Kruk, M.R., and Stanley, B.G. (2019). Editorial: Current Views of Hypothalamic Contributions to the Control of Motivated Behaviors. Frontiers in systems neuroscience *13*. 10.3389/fnsys.2019.00032.
43. Dulac, C., O'Connell, L.A., and Wu, Z. (2014). Neural control of maternal and paternal behaviors. Science *345*, 765-770. 10.1126/science.1253291.
44. Basu, J., and Siegelbaum, S.A. (2015). The Corticohippocampal Circuit, Synaptic Plasticity, and Memory. Cold Spring Harb Perspect Biol *7*. 10.1101/cshperspect.a021733.
45. Aoi, M.C., Mante, V., and Pillow, J.W. (2020). Prefrontal cortex exhibits multidimensional dynamic encoding during decision-making. Nature neuroscience *23*, 1410-1420. 10.1038/s41593-020-0696-5.
46. Sarel, A., Palgi, S., Blum, D., Aljadeff, J., Las, L., and Ulanovsky, N. (2022). Natural switches in behaviour rapidly modulate hippocampal coding. Nature *609*, 119-127. 10.1038/s41586-022-05112-2.
47. Kim, J., Joshi, A., Frank, L., and Ganguly, K. (2023). Cortical-hippocampal coupling during manifold exploration in motor cortex. Nature *613*, 103-110. 10.1038/s41586-022-05533-z.
48. Steinmetz, N.A., Zatka-Haas, P., Carandini, M., and Harris, K.D. (2019). Distributed coding of choice, action and engagement across the mouse brain. Nature *576*, 266-+. 10.1038/s41586-019-1787-x.
49. Allen, W.E., Chen, M.Z., Pichamoorthy, N., Tien, R.H., Pachitariu, M., Luo, L.Q., and Deisseroth, K. (2019). Thirst regulates motivated behavior through modulation of brainwide neural population dynamics. Science *364*, 253-+. 10.1126/science.aav3932.
50. Kennedy, A., Kunwar, P.S., Li, L.Y., Stagkourakis, S., Wagenaar, D.A., and Anderson, D.J. (2020). Stimulus-specific hypothalamic encoding of a persistent defensive state. Nature *586*, 730-734. 10.1038/s41586-020-2728-4.
51. Yang, T., Yang, C.F., Chizari, M.D., Maheswaranathan, N., Burke, K.J., Borius, M., Inoue, S., Chiang, M.C., Bender, K.J., Ganguli, S., and Shah, N.M. (2017). Social Control of Hypothalamus-Mediated Male Aggression. Neuron *95*, 955-+. 10.1016/j.neuron.2017.06.046.
52. Ishii, K.K., Osakada, T., Mori, H., Miyasaka, N., Yoshihara, Y., Miyamichi, K., and Touhara, K. (2017). A Labeled-Line Neural Circuit for Pheromone-Mediated Sexual Behaviors in Mice. Neuron *95*, 123-+. 10.1016/j.neuron.2017.05.038.
53. Falkner, A.L., Grosenick, L., Davidson, T.J., Deisseroth, K., and Lin, D.Y. (2016). Hypothalamic control of male aggression-seeking behavior. Nature neuroscience *19*, 596-+. 10.1038/nn.4264.
54. Lee, H., Kim, D.W., Remedios, R., Anthony, T.E., Chang, A., Madisen, L., Zeng, H.K., and Anderson, D.J. (2014). Scalable control of mounting and attack by Esr1⁺ neurons in the ventromedial hypothalamus. Nature *509*, 627-+. 10.1038/nature13169.
55. Yang, C.F., Chiang, M.C., Gray, D.C., Prabhakaran, M., Alvarado, M., Juntti, S.A., Unger, E.K., Wells, J.A., and Shah, N.M. (2013). Sexually Dimorphic Neurons in the Ventromedial Hypothalamus Govern Mating in Both Sexes and Aggression in Males. Cell *153*, 896-909. 10.1016/j.cell.2013.04.017.

56. Liu, D., Rahman, M., Johnson, A., Tsutsui-Kimura, I., Pena, N., Talay, M., Logeman, B.L., Finkbeiner, S., Choi, S., Capo-Battaglia, A., et al. (2023). A Hypothalamic Circuit Underlying the Dynamic Control of Social Homeostasis. bioRxiv. 10.1101/2023.05.19.540391.
57. Stagkourakis, S., Smiley, K.O., Williams, P., Kakadellis, S., Ziegler, K., Bakker, J., Brown, R.S.E., Harkany, T., Grattan, D.R., and Broberger, C. (2020). A Neuro-hormonal Circuit for Paternal Behavior Controlled by a Hypothalamic Network Oscillation. Cell *182*, 960-+. 10.1016/j.cell.2020.07.007.
58. Mei, L., Yan, R.Z., Yin, L.P., Sullivan, R.M., and Lin, D.Y. (2023). Antagonistic circuits mediating infanticide and maternal care in female mice. Nature. 10.1038/s41586-023-06147-9.
59. Zhang, S.X., Lutas, A., Yang, S., Diaz, A., Fluhr, H., Nagel, G., Gao, S.Q., and Andermann, M.L. (2021). Hypothalamic dopamine neurons motivate mating through persistent cAMP signalling. Nature *597*, 245-+. 10.1038/s41586-021-03845-0.
60. Kohl, J., and Dulac, C. (2018). Neural control of parental behaviors. Current opinion in neurobiology *49*, 116-122. 10.1016/j.conb.2018.02.002.
61. Kira, S., Safaai, H., Morcos, A.S., Panzeri, S., and Harvey, C.D. (2023). A distributed and efficient population code of mixed selectivity neurons for flexible navigation decisions. Nature communications *14*, 2121. 10.1038/s41467-023-37804-2.
62. Kaufman, M.T., Benna, M.K., Rigotti, M., Stefanini, F., Fusi, S., and Churchland, A.K. (2022). The implications of categorical and category-free mixed selectivity on representational geometries. Current opinion in neurobiology *77*, 102644. 10.1016/j.conb.2022.102644.
63. Johnston, W.J., Palmer, S.E., and Freedman, D.J. (2020). Nonlinear mixed selectivity supports reliable neural computation. PLoS computational biology *16*, e1007544. 10.1371/journal.pcbi.1007544.
64. Grunfeld, I.S., and Likhtik, E. (2018). Mixed selectivity encoding and action selection in the prefrontal cortex during threat assessment. Current opinion in neurobiology *49*, 108-115. 10.1016/j.conb.2018.01.008.
65. Rigotti, M., Barak, O., Warden, M.R., Wang, X.J., Daw, N.D., Miller, E.K., and Fusi, S. (2013). The importance of mixed selectivity in complex cognitive tasks. Nature *497*, 585-590. 10.1038/nature12160.
66. Schoonover, C.E., Ohashi, S.N., Axel, R., and Fink, A.J.P. (2021). Representational drift in primary olfactory cortex. Nature *594*, 541-546. 10.1038/s41586-021-03628-7.
67. Zhao, P., Chen, X., Bellafard, A., Murugesan, A., Quan, J., Aharoni, D., and Golshani, P. (2023). Accelerated social representational drift in the nucleus accumbens in a model of autism. bioRxiv. 10.1101/2023.08.05.552133.
68. Haimerl, C., Savin, C., and Simoncelli, E.P. (2019). Flexible information routing in neural populations through stochastic comodulation. Advances in Neural Information Processing Systems 32 (Nips 2019) *32*.
69. Guo, Z., Yin, L., Diaz, V., Dai, B., Osakada, T., Lischinsky, J.E., Chien, J., Yamaguchi, T., Urtecho, A., Tong, X., et al. (2023). Neural dynamics in the limbic system during male social behaviors. Neuron. 10.1016/j.neuron.2023.07.011.
70. Segalin, C., Williams, J., Karigo, T., Hui, M., Zelikowsky, M., Sun, J.J., Perona, P., Anderson, D.J., and Kennedy, A. (2021). The Mouse Action Recognition System (MARS) software pipeline for automated analysis of social behaviors in mice. eLife *10*. 10.7554/eLife.63720.
71. Jun, J.J., Steinmetz, N.A., Siegle, J.H., Denman, D.J., Bauza, M., Barbarits, B., Lee, A.K., Anastassiou, C.A., Andrei, A., Aydin, C., et al. (2017). Fully integrated silicon probes for high-density recording of neural activity. Nature *551*, 232-+. 10.1038/nature24636.
72. Lundberg, S.M., and Lee, S.I. (2017). A Unified Approach to Interpreting Model Predictions. Adv Neur In *30*.
73. Chen, T.Q., and Guestrin, C. (2016). XGBoost: A Scalable Tree Boosting System. Kdd'16: Proceedings of the 22nd Acm Sigkdd International Conference on Knowledge Discovery and Data Mining, 785-794. 10.1145/2939672.2939785.

Acknowledgments

Members of the Anderson laboratory are thanked for their advice and discussion during the preparation of this manuscript. Light-sheet imaging was performed in the Biological Imaging Facility, with the support of the Caltech Beckman Institute and the Arnold and Mabel Beckman Foundation. Special thanks to the Director of the Biological Imaging Facility at Caltech, Dr. Andres Collazo, for providing crucial experimental support and advice. We also thank Jung-Sook Chang and Xiaolin Da for experimental support, C. Chiu for laboratory management, G. Mancuso, L. Chavarria and D. R. Navarrete for administrative assistance. S.S. received support from the Wenner-Gren Foundations and by NIH K99MH131754. D.J.A. is an investigator of the Howard Hughes Medical Institute. This work was supported in part by NIH grants NS123916, MH1223612, and MH070053 to D.J.A. The content is solely the responsibility of the authors and does not necessarily represent the official views of the National Institutes of Health. All authors support an inclusive, diverse, and equitable conduct of research.

Author contributions

S.S. conceived the study, designed and performed all experiments, wrote hardware-operating and analysis code, analyzed data, and generated the first draft of the manuscript. G.S. contributed to brain clearing, light-sheet microscopy, and silicon probe registration to the Allen Common Coordinate Framework. M.M. performed the decoding analysis using gradient boosted trees. P.P. designed decoding approaches. M.F. wrote and provided code for image registration for light-sheet microscopy data. J.K. contributed to the analysis. M.P. supervised S.S.. D.J.A. supervised S.S., contributed to the study design and analysis, and wrote the manuscript. All authors reviewed the manuscript.

Competing interests

The authors declare no competing financial interests.

Main Figures

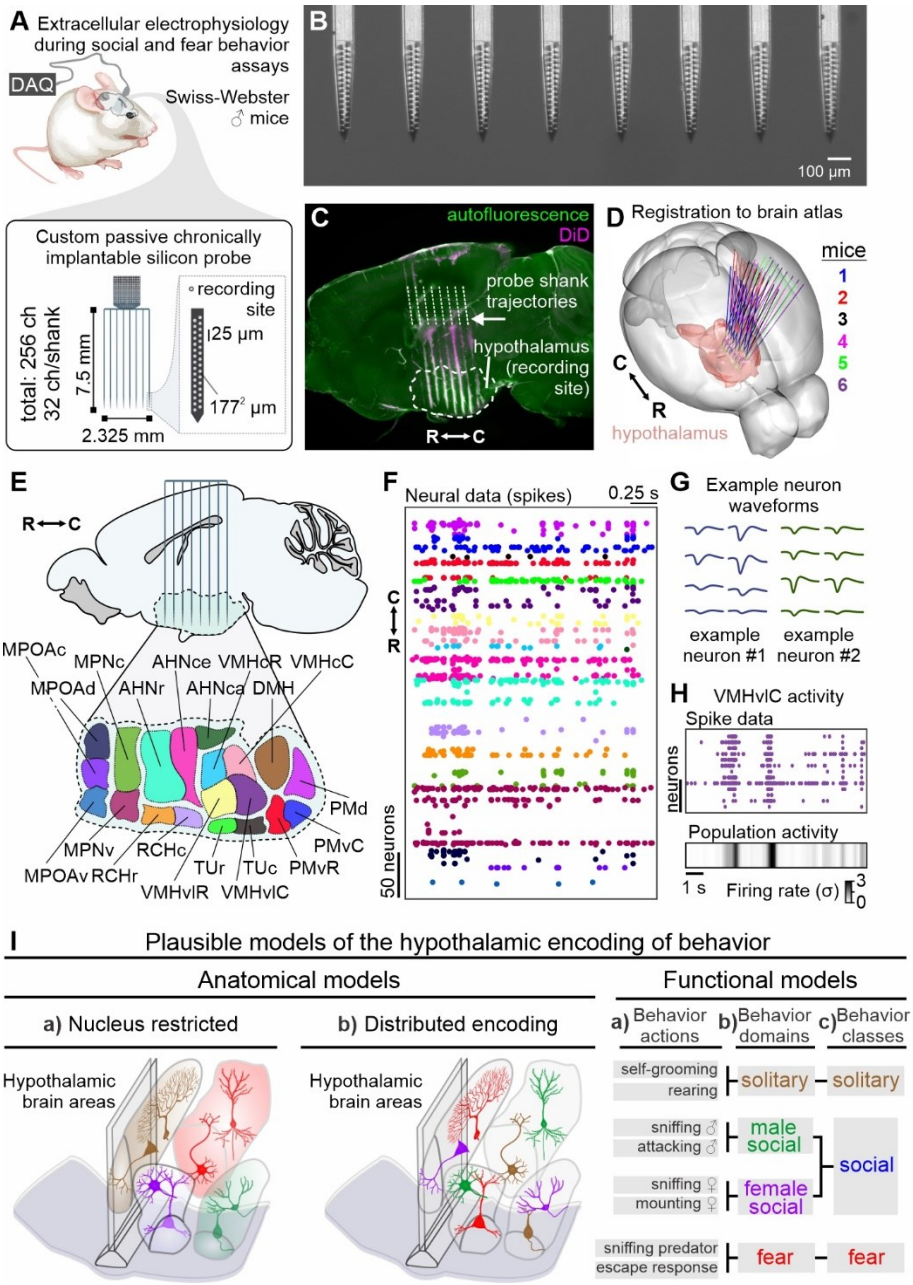

Figure 1. Approach for single neuron recordings across the hypothalamus using custom extracellular electrophysiology silicon probes in freely moving mice.

(A) Top - outbred Swiss Webster male mice were chronically implanted with a custom silicon probe. Bottom - design, and specifics of the eight-shank 256-channel custom silicon probe manufactured by NeuroNexus.

(B) Stereoscope-acquired image of the shank-tips of the probe containing the microelectrodes.

601 (C) Post-hoc identification of probe shanks and electrode placement through volumetric light-sheet
602 imaging.
603 (D) Registration of the probes to the Allen Common Coordinate Framework across all recorded mice.
604 (E) Target coordinates include twenty, individually colored subregions of the hypothalamus.
605 (F) Following electrode mapping and spike sorting, single neurons were assigned to their respective
606 locations / hypothalamic areas.
607 (G) Example waveforms of two recorded neurons.
608 (H) Example spike data across thirteen neurons of VMHvl (top), and illustration of their average activity
609 (bottom).
610 (I) Spatial and functional plausible models, combination of which could explain the hypothalamic encoding
611 of behavior.
612 Abbreviations: DAQ: data acquisition system, MPOAv: medial preoptic area – ventral subdivision.
613 MPOAc: medial preoptic area – central subdivision. MPOAd: medial preoptic area – dorsal subdivision.
614 MPNv: medial preoptic nucleus – ventral subdivision. MPNc: medial preoptic nucleus – central
615 subdivision. RCHr: retrochiasmatic area – rostral subdivision. RCHc: retrochiasmatic area – caudal
616 subdivision. AHNr: anterior hypothalamic nucleus – rostral subdivision. AHNce: anterior hypothalamic
617 nucleus – central subdivision. AHNca: anterior hypothalamic nucleus – caudal subdivision. TUr: tuberal
618 nucleus – rostral subdivision. TUc: tuberal nucleus – caudal subdivision. VMHvlR: ventromedial
619 hypothalamic nucleus ventrolateral segment – rostral subdivision. VMHvlC: ventromedial hypothalamic
620 nucleus ventrolateral segment – caudal subdivision. VMHcR: ventromedial hypothalamic nucleus central
621 segment – rostral subdivision. VMHcC: ventromedial hypothalamic nucleus central segment – caudal
622 subdivision. DMH: dorsomedial hypothalamic nucleus. PMvR: ventral premammillary nucleus – rostral
623 subdivision. PMvC: ventral premammillary nucleus – caudal subdivision. PMd: dorsal premammillary
624 nucleus. See also Figures S1 and S2.

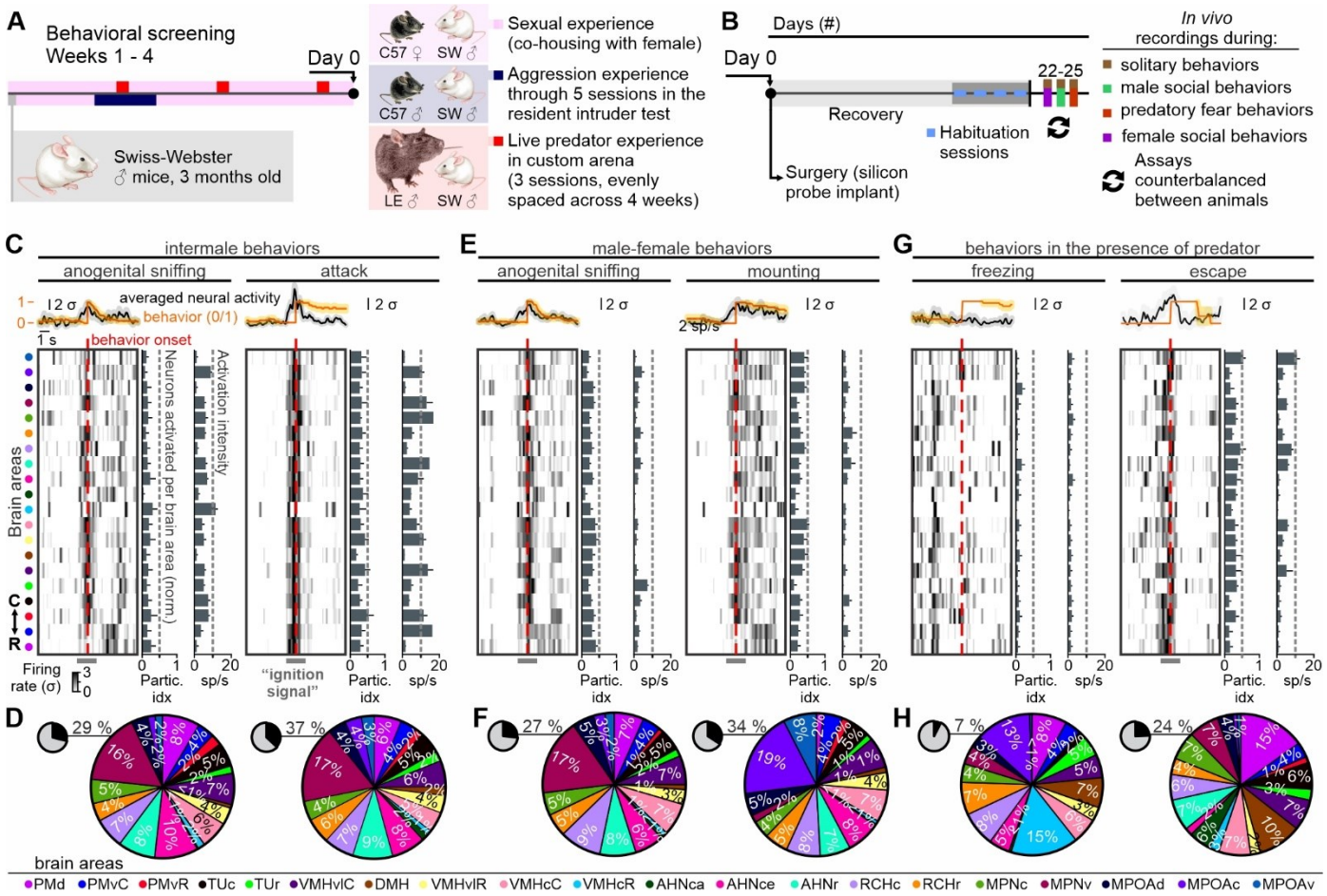

Figure 2. Neural ignition signals dominate the peri-onset interval of all instinctual behaviors, apart from freezing to the presence of a predator.

(A) Behavioral screening of outbred Swiss Webster mice was used to identify individual mice with prominent behavioral expressions in all of the three behavior paradigms of interest used to assess mating with a female conspecific, aggression against a male conspecific and fear behaviors in the presence of a predator (Long-Evans [LE] rat). Only mice that exhibited appetitive and consummatory behaviors across the three behavior domains (i.e., mating, aggression, and fear), across all behavior screening sessions were selected for chronic silicon probe implant surgery.

(B) Schematic illustrating the timeline following implantation of the silicon probe. Animals were allowed to fully recover for two weeks in their home cage and were given access to a running wheel. Four

habituation sessions were performed (one daily), 4 days prior to the start of the neural recordings and behavior experiments. Habitation sessions included exposure to the exact experimental conditions, in the absence of the stimulus (conspecific, or predator).

(C) Average behavior signal and mean neural activity at the peri-onset interval of an appetitive and a consummatory intermale social behavior (top). Average neural activity per nucleus (heatmap), participation index (% of neurons activated above 2 SD from baseline activity), and average firing rate of the activated neurons (bottom, n = 6 mice, neural data averaged across three consecutive behavior instances per mouse).

(D) Small black and gray pie plot: Black – total % of neurons activated, Gray: total % of neurons that did not raise their activity above 2σ. Larger colored pie plot illustrates the spatial coordinates of the neurons that became active (raised their activity >2σ), during male anogenital sniffing (left) and intermale attack (right, n = 6 mice, neural data averaged across three consecutive behavior instances).

(E and F) Same as panels (C) and (D) for an appetitive and a consummatory male-female social behavior.

(G and H) Same as panels (C) and (D) for two predatory fear behaviors.

In box-and-whisker plots, center lines indicate medians, box edges represent the interquartile range, and whiskers extend to the minimal and maximal values. See also Figures S3, S4, and S5. Abbreviations: Partic. Idx.: participation index, sp/s: Firing rate (spikes / sec). Abbreviations of brain areas are described on the legend of Figure 1.

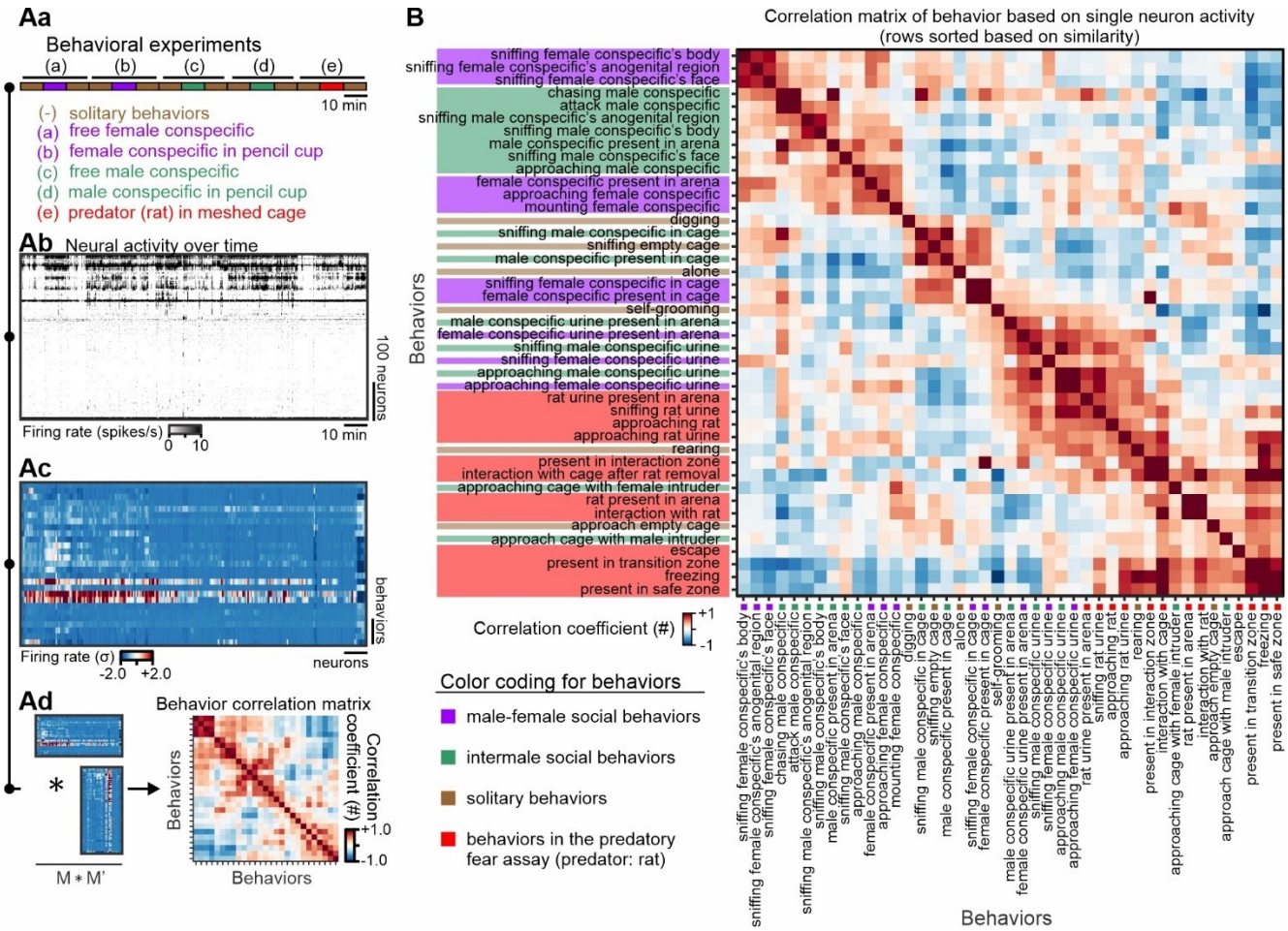

Figure 3. Non-overlapping encoding of social and fear behavior classes by hypothalamic neurons.

(A) Analysis design to generate a behaviors correlation matrix.

(Aa) Experimental conditions.

(Ab) Single-unit neural activity during the behavioral paradigms shown in Aa.

(Ac) Z-scored activity of all recorded neurons across solitary-, social-, and fear-behaviors (data from an example mouse).

(Ad) Multiplication of the matrix shown in ac with its transposed version, results to the behavior covariance matrix, which is then transformed to a behavior correlation matrix.

(B) Correlation matrix of behavior (average across n = 6 mice).

Correlation matrices of behavior of the individual mice can be found in Figure S7.

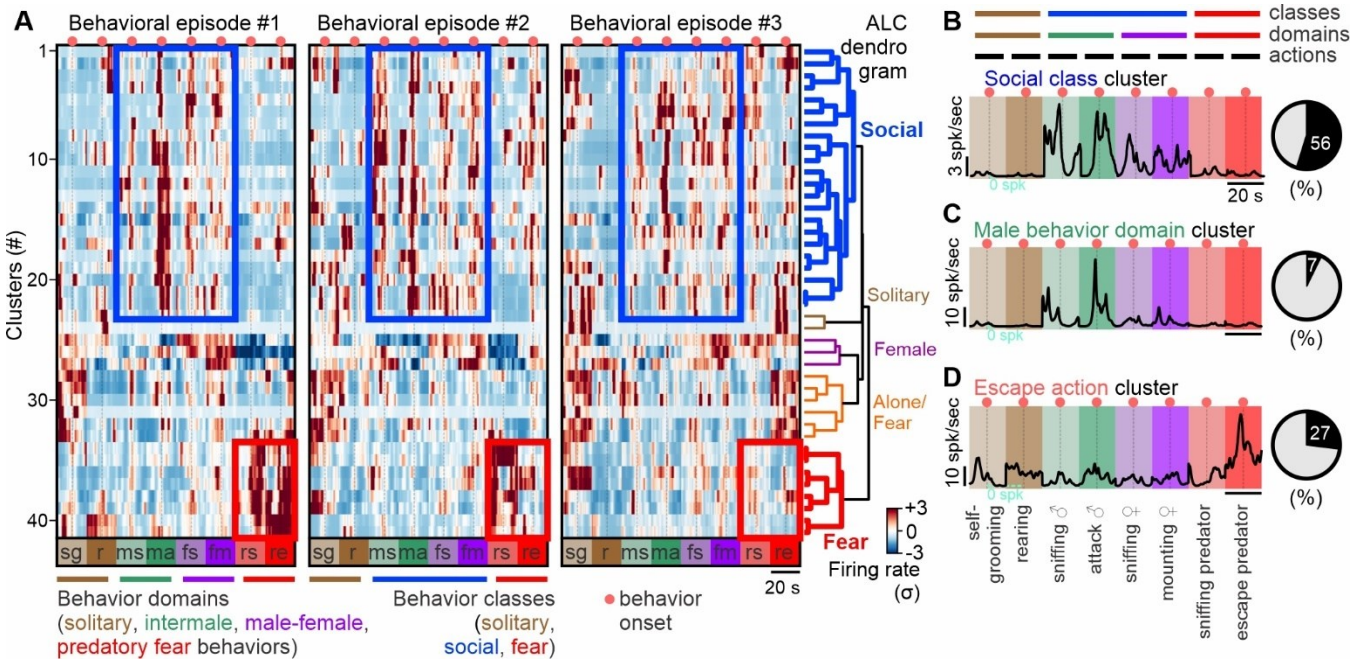

Figure 4. Distinct hypothalamic neuron ensembles encode social and fear behavior classes.

(A) Mean activity of *k*-means clusters explaining 70% of the variance of the single unit data (Extended Data Figure 8). Clusters are sorted using agglomerative linkage clustering to generate a dendrogram whose branches have been assigned semantic labels, based on cluster activity being higher than two standard deviations in specific behavioral classes.

(B) Left: Mean activity of a *k*-means cluster selected from the forty-one clusters identified and shown in (Figure 4A), exhibiting mixed selectivity, i.e., activity in diverse behavior domains – in this case, in male-male and male-female behaviors. Right: Portion of clusters showing mixed-selectivity / multi-domain activity.

(C) Left: Mean activity of a *k*-means cluster selected from the forty-one clusters identified (Figure 4A), showing mixed selectivity within a behavioral domain – in this case, in intermale behaviors. Right: Portion of clusters showing mixed selectivity within a behavioral domain (alone / intermale / male-female / and fear behaviors).

679 (D) Left: Mean activity of a *k*-means cluster selected from the forty-one clusters identified (Figure 4A),
680 showing behavior-specific tuning – in this case, in escape response to a predator. Right: Portion of
681 clusters showing behavior action-specific tuning.
682 Abbreviations: sg: self-grooming, r: rearing, ms: male intruder anogenital sniffing, ma: intermale attack,
683 fs: female intruder anogenital sniffing, fm: mounting female intruder, rs: sniffing predator, re: escape
684 response to a predator. See also Figures S8, and S9.

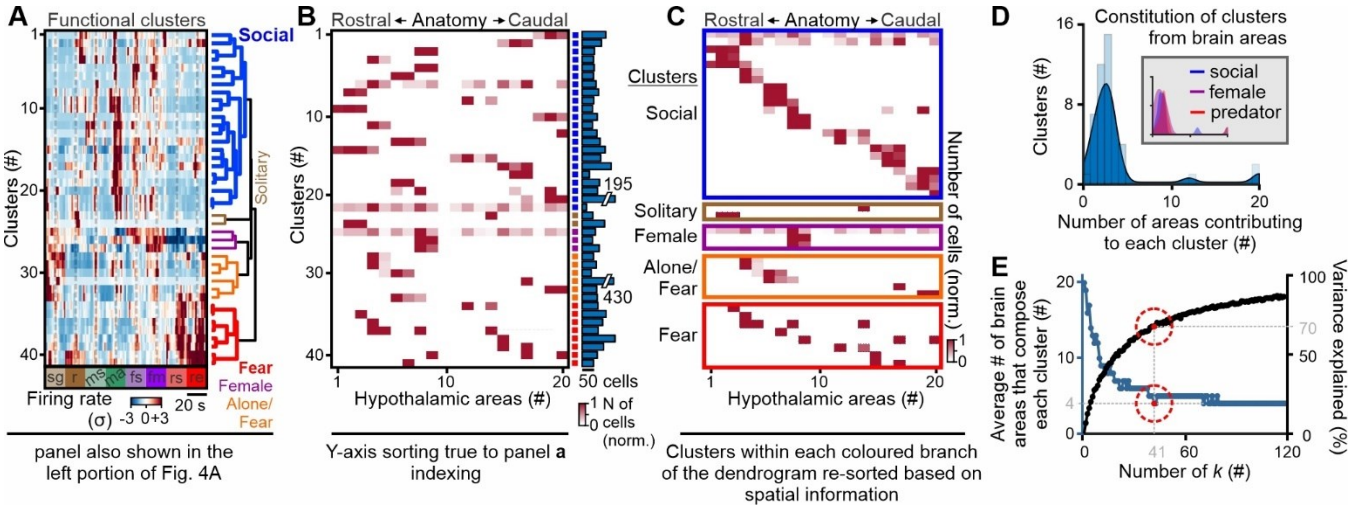

Figure 5. Encoding of behavior classes is spatially distributed, but single clusters are spatially localized.

(A) Functional clusters of single neuron activity (panel from Figure 4A – left).

(B) Spatial composition of each of the 41 functional clusters shown in panel (A).

(C) Re-sorting the spatial composition of each cluster, to present clusters composed of most rostral regions, to clusters composed of most caudal regions.

(D) Histogram of hypothalamic area contribution per cluster. Inset: Histogram of hypothalamic area contribution to clusters that are active in specific behaviors.

(E) Spatial composition of clusters based on the choice of *k* (number of clusters selected for *k*-means clustering), reveals that the average composition of a cluster by four regions is a stable solution.

Abbreviations: sg: self-grooming, r: rearing, ms: male intruder anogenital sniffing, ma: intermale attack, fs: female intruder anogenital sniffing, fm: mounting female intruder, rs: sniffing predator, re: escape response to a predator. See also Figures S9B-S9D.

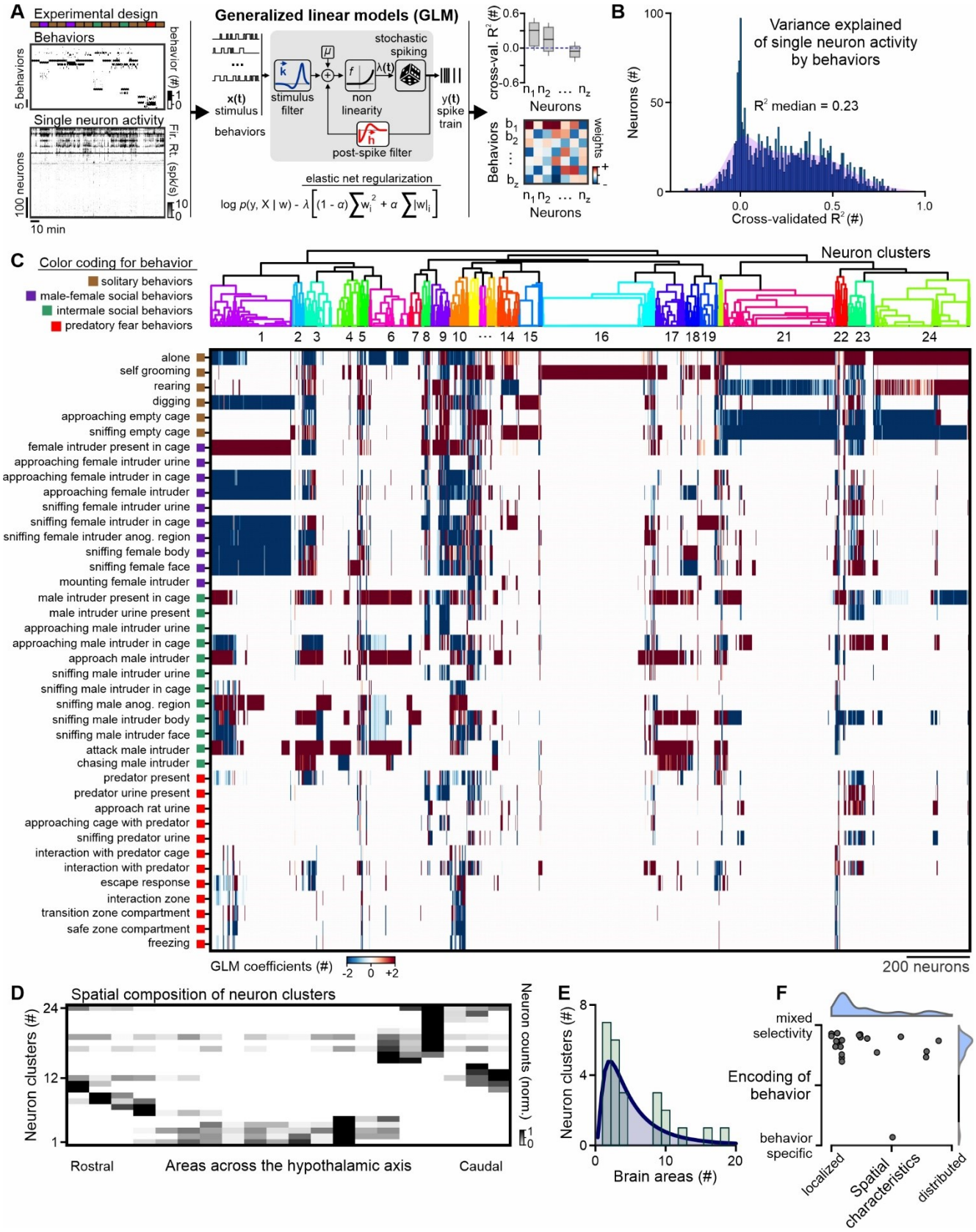
A
Experimental design
Behaviors
5 behaviors
behavior (#)
Single neuron activity
100 neurons
Fir. Rt. (spk/s)
10 min
Generalized linear models (GLM)
x(t) stimulus
behaviors
stimulus filter
non linearity
stochastic spiking
post-spike filter
y(t) spike train
elastic net regularization
log p(y, X | w) - λ[(1 - α)∑w_i^2 + α∑|w|_i]
cross-val. R² (#)
Neurons
Behaviors
weights
B
Variance explained of single neuron activity by behaviors
R² median = 0.23
Neurons (#)
Cross-validated R² (#)
C
Color coding for behavior
solitary behaviors
male-female social behaviors
intermale social behaviors
predatory fear behaviors
Neuron clusters
alone
self grooming
rearing
digging
approaching empty cage
sniffing empty cage
female intruder present in cage
approaching female intruder urine
approaching female intruder in cage
approaching female intruder
sniffing female intruder urine
sniffing female intruder in cage
sniffing female intruder anog. region
sniffing female body
sniffing female face
mounting female intruder
male intruder present in cage
male intruder urine present
approaching male intruder urine
approaching male intruder in cage
approach male intruder
sniffing male intruder urine
sniffing male intruder in cage
sniffing male anog. region
sniffing male intruder body
sniffing male intruder face
attack male intruder
chasing male intruder
predator present
predator urine present
approach rat urine
approaching cage with predator
sniffing predator urine
interaction with predator cage
interaction with predator
escape response
interaction zone
transition zone compartment
safe zone compartment
freezing
GLM coefficients (#)
200 neurons
D
Spatial composition of neuron clusters
Neuron clusters (#)
Neuron counts (norm.)
Rostral
Areas across the hypothalamic axis
Caudal
E
Neuron clusters (#)
Brain areas (#)
F
mixed selectivity
Encoding of behavior
behavior specific
localized
Spatial characteristics
distributed

699

700 **Figure 6. Solitary, social, and fear behaviors explain a quarter of hypothalamic neuron activity**
701 **variance and clustering of encoding model weights suggest anatomical organization of functional**
702 **neuron clusters.**
703 (A) Analysis design using generalized linear models (GLMs) to study the encoding of behavior by non-
704 genetically defined mesoscale hypothalamic populations.
705 (B) Variance explained (cross-validated, shuffled data R^2 subtracted, R^2) of single-neuron activity (n=6
706 mice, 2347 neurons) based on forty-two instinctual behaviors.
707 (C) Agglomerative linkage clustering of behavior GLM-generated coefficients into twenty-four neural
708 dendrogram branches/clusters.
709 (D) Average neuron counts per brain area across the hypothalamic rostro-caudal axis across all neural
710 branches, reveals a spatial bias of neural branch composition.
711 (E) Histogram of hypothalamic area contribution per cluster.
712 (F) Spatial vs. functional characteristics of neuron clusters.
713 In box-and-whisker plots, center lines indicate medians, box edges represent the interquartile range, and
714 whiskers extend to the minimal and maximal values. See also Figures S11, S12, and S13.

Supplemental Figures

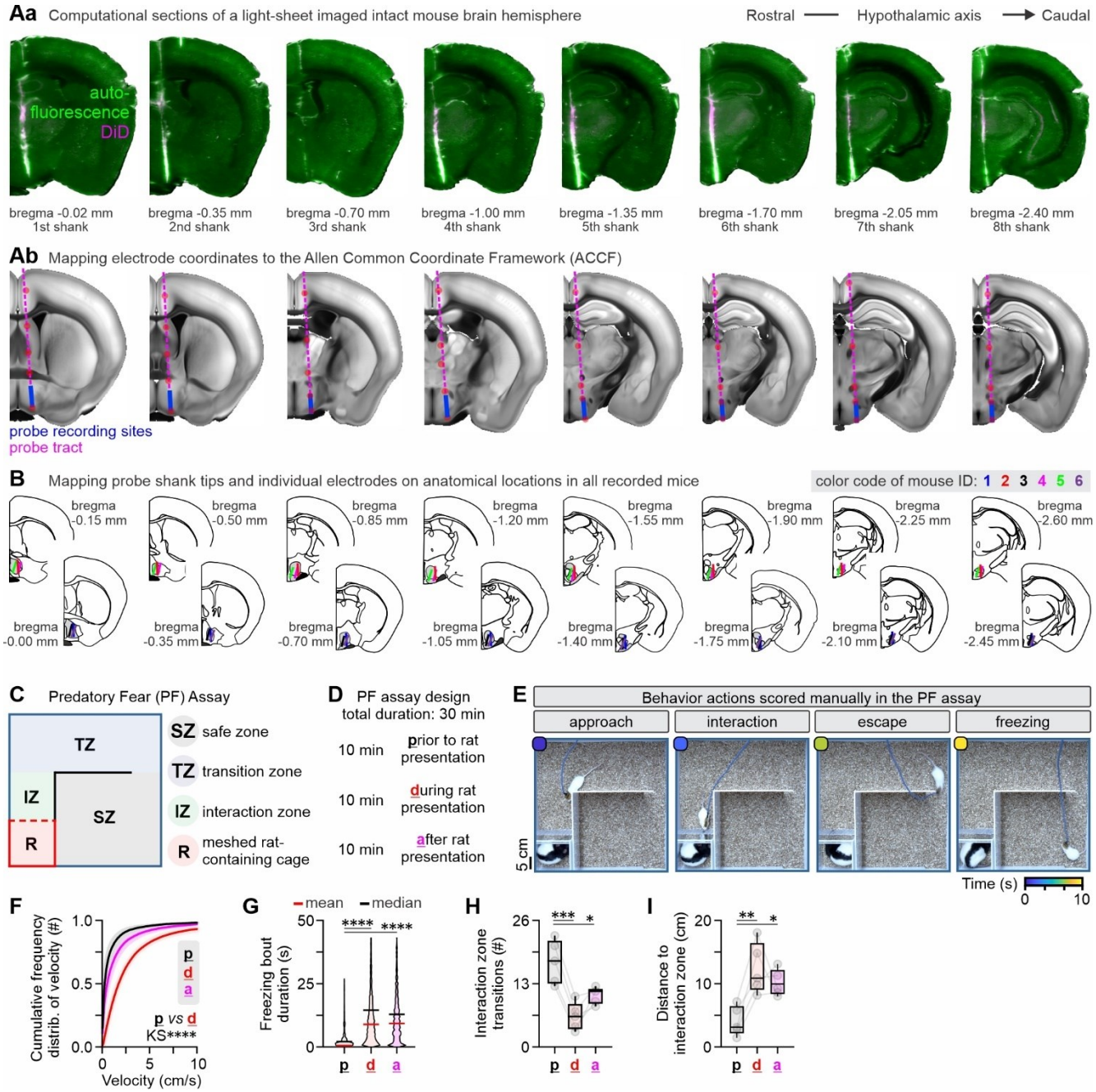

Figure S1. Mapping of recording sites across the rostrocaudal axis of the hypothalamus, and quantification of behavior in the predatory fear assay, related to Figures 1 and 2

(Aa) Computationally sectioned coronal views of the mouse brain that include each of the eight shanks of the chronic silicon probe implant in an example mouse brain.

(Ab) Mapping the shank and the electrode-containing area of the shank to the Allen Common Coordinate Framework (example sections/mouse).

(B) Mapping the overlap of all recording electrodes of each of the eight shanks across all probes/mice to the hypothalamic areas (n=6 mice).

(C) Experimental design of a custom predatory fear assay, with four compartments. R: compartment containing the predator (rat), with a single, clear, and perforated side facing the compartment IZ, i.e., interaction compartment. TZ: is the transition compartment that links compartments R and SZ, the latter furthest away from the predator.

(D) Timeline of the behavioral experiments with the fear condition flanked by two periods where the implanted mouse is alone in the arena.

(E) Snapshots illustrating four manually annotated behaviors, specifically; approaching the predator, interacting with the predator, escape response to a predator (a high-velocity activity bout towards the safe zone compartment), and freezing behavior (observed in the freezing compartment).

(F) Frequency distribution of velocity during the three conditions shown in panel (B).

(G) Freezing bout duration in the three conditions presented in in panel (B).

(H) Number of crosses of the interaction zone across the three conditions presented in panel (B).

(I) Distance to interaction zone among the three conditions presented in panel (B).

*$P < 0.05$, **$P < 0.01$, ***$P < 0.001$, ****$P < 0.0001$. Statistical comparisons of the data illustrated in panel (F) were performed by the Kolmogorov-Smirnov test, while comparisons of the data shown in panels (G-I) were performed through One-Way ANOVA and Dunnett's post-hoc test was used to correct for multiple comparisons. In box-and-whisker plots, center lines indicate medians, box edges represent the interquartile range, and whiskers extend to the minimal and maximal values.

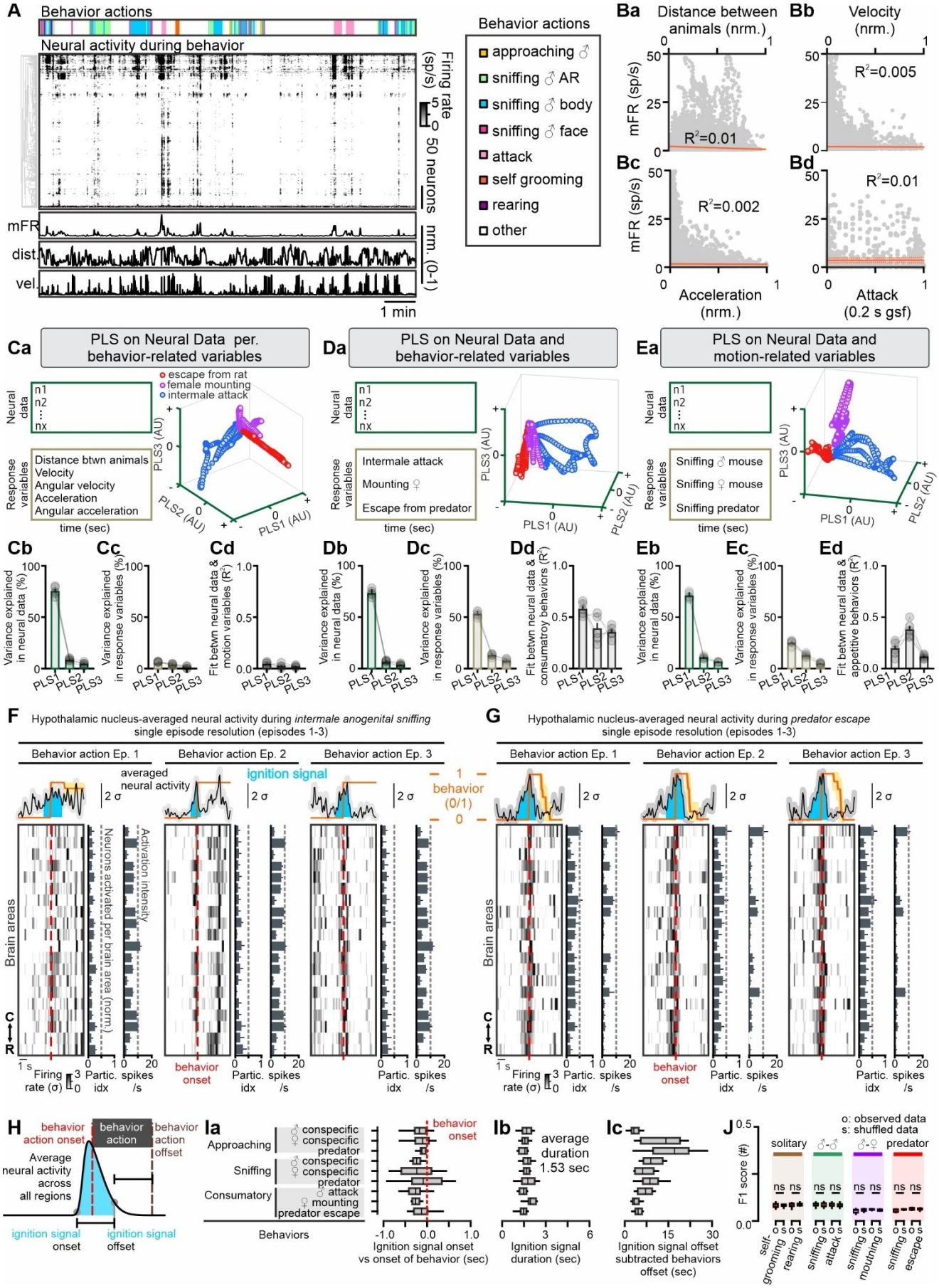
A
Behavior actions
Neural activity during behavior
Firing rate (sp/s)
50 neurons
mFR
dist.
vel.
nrm. (0-1)
1 min
Behavior actions
approaching ♂
sniffing ♂ AR
sniffing ♂ body
sniffing ♂ face
attack
self grooming
rearing
other
Ba
Distance between animals (nrm.)
Bb
Velocity (nrm.)
Bc
Bd
mFR (sp/s)
R²=0.01
R²=0.005
R²=0.002
R²=0.01
Acceleration (nrm.)
Attack (0.2 s gsf)
Ca
PLS on Neural Data per. behavior-related variables
Da
PLS on Neural Data and behavior-related variables
Ea
PLS on Neural Data and motion-related variables
Neural data
n1
n2
nx
Response variables
Distance btwn animals
Velocity
Angular velocity
Acceleration
Angular acceleration
Intermale attack
Mounting ♀
Escape from predator
Sniffing ♂ mouse
Sniffing ♀ mouse
Sniffing predator
time (sec)
escape from rat
female mounting
intermale attack
PLS1 (AU)
PLS2 (AU)
PLS3 (AU)
Cb
Cc
Cd
Db
Dc
Dd
Eb
Ec
Ed
Variance explained in neural data (%)
Variance explained in response variables (%)
Fit betwn neural data & motion variables (R²)
Fit betwn neural data & consumatroy behaviors (R²)
Fit betwn neural data & appetitive behaviors (R²)
PLS1
PLS2
PLS3
F
Hypothalamic nucleus-averaged neural activity during intermale anogenital sniffing
single episode resolution (episodes 1-3)
G
Hypothalamic nucleus-averaged neural activity during predator escape
single episode resolution (episodes 1-3)
Behavior action Ep. 1
Behavior action Ep. 2
Behavior action Ep. 3
averaged neural activity
ignition signal
behavior (0/1)
2 σ
Brain areas
Neurons activated per brain area (norm.)
Activation intensity
behavior onset
Firing rate (σ)
Partic. idx
spikes /s
H
behavior action onset
behavior action
behavior action offset
Average neural activity across all regions
ignition signal onset
ignition signal offset
Ia
Approaching
Sniffing
Consumatory
conspecific
predator
attack
mounting
predator escape
Behaviors
Ignition signal onset vs onset of behavior (sec)
Ib
average duration 1.53 sec
Ignition signal duration (sec)
Ic
Ignition signal offset subtracted behaviors offset (sec)
J
o: observed data
s: shuffled data
solitary
♂-♂
♂-♀
predator
F1 score (#)
ns
self-grooming
rearing
sniffing attack
sniffing mounting
sniffing escape

746

Figure S2. Behaviors but not motion-related variables correlate with hypothalamic neuron firing rate, and ignition signal parameter analysis, related to Figure 2

(A) Example time series data of behavior, single neuron activity, mean firing rate, distance between animals, and velocity of recorded mouse.

(Ba) Linear regression between mean firing rate and distance between animals (data from six mice).

(Bb) Linear regression between mean firing rate and velocity of the recorded mouse (data from six mice).

(Bc) Linear regression between mean firing rate and acceleration of recorded mouse (data from six mice).

(Bd) Linear regression between mean firing rate and intermale attack behavior (data from six mice).

(Ca) Left: Analysis design and input to partial least-squares regression, to assess the correlation between partial least-square components between neural data and motion-related variables. Right: Neural trajectories of PLS components in the PLS space (example mouse).

(Cb) Variance explained by PLS components of the single-unit neural data (n=6 mice).

(Cc) Variance explained by PLS components of the motion-related variables (n=6 mice).

(Cd) Fit between neural and motion-variable PLS components, indicative of a poor link between the two types of data (n=6 mice).

(Da) Left: Analysis design and input to partial least-squares regression, to assess the correlation between partial least-square components between neural data and consummatory social and fear behaviors. Right: Neural trajectories of PLS components in the PLS space (example mouse).

(Db) Variance explained by PLS components of the single-unit neural data(n=6 mice).

(Dc) Variance explained by PLS components of the consummatory social and fear behaviors (n=6 mice).

(Dd) Fit between neural and consummatory instinctual behavior-based PLS components, indicative of a link between the two types of data (n=6 mice).

(Ea) Left: Analysis design and input to partial least-squares regression, to assess the correlation between partial least-square components between neural data and appetitive social and fear behaviors. Right: Neural trajectories of PLS components in the PLS space (example mouse).

(Eb) Variance explained by PLS components of the single-unit neural data(n=6 mice).

773 (Ec) Variance explained by PLS components of the appetitive social and fear behaviors (n=6 mice).
774 (Ed) Fit between neural and appetitive social and fear behavior-based PLS components, indicative of a
775 moderate link between the two types of data (n=6 mice).
776 (F) Top part: Average behavior signal and mean neural activity at the peri-onset interval of sniffing a male
777 conspecific across three behavioral episodes. Color plot part: Average neural activity per nucleus
778 (heatmap), participation index (% of neurons activated above 2 SD from baseline activity), and average
779 firing rate of the activated neurons (bottom, n = 6 mice, in three behavior episodes per mouse).
780 (G) Top part: Average behavior signal and mean neural activity at the peri-onset interval of escape
781 responses in the presence of a predator, in three behavioral episodes. Color plot part: Average neural
782 activity per nucleus (heatmap), participation index (% of neurons activated above 2 SD from baseline
783 activity), and average firing rate of the activated neurons (bottom, n = 6 mice, in three behavior episodes
784 per mouse).
785 (H) Characteristics of ignition signals include onset, offset, and duration relevant to behavior.
786 (Ia) Quantification of the onset of ignition signals relevant to the onset of behavior (n = 6 mice, neural
787 data averaged across three consecutive behavior instances per mouse).
788 (Ib) Quantification of the ignition signal duration (n = 6 mice, neural data averaged across three
789 consecutive behavior instances per mouse).
790 (Ic) Quantification of the ignition signal offset subtracted behavior offset (n = 6 mice, neural data averaged
791 across three consecutive behavior instances per mouse).
792 (J) SVM decoder F1 score on behavior actions of interest based on nucleus-averaged neural activity (n
793 = 6 mice).
794 Abbreviations: mFR: mean firing rate all recorded neurons, dist.: distance between animals, vel.: velocity,
795 sp/s: spikes per second, nrm.: data normalized between 0 and 1 values, 0.2 s gsf: 200 millisecond
796 Gaussian smoothing filter applied on the spike and behavior data prior to performing linear regression.
797 In box-and-whisker plots, center lines indicate medians, box edges represent the interquartile range, and
798 whiskers extend to the minimal and maximal values.

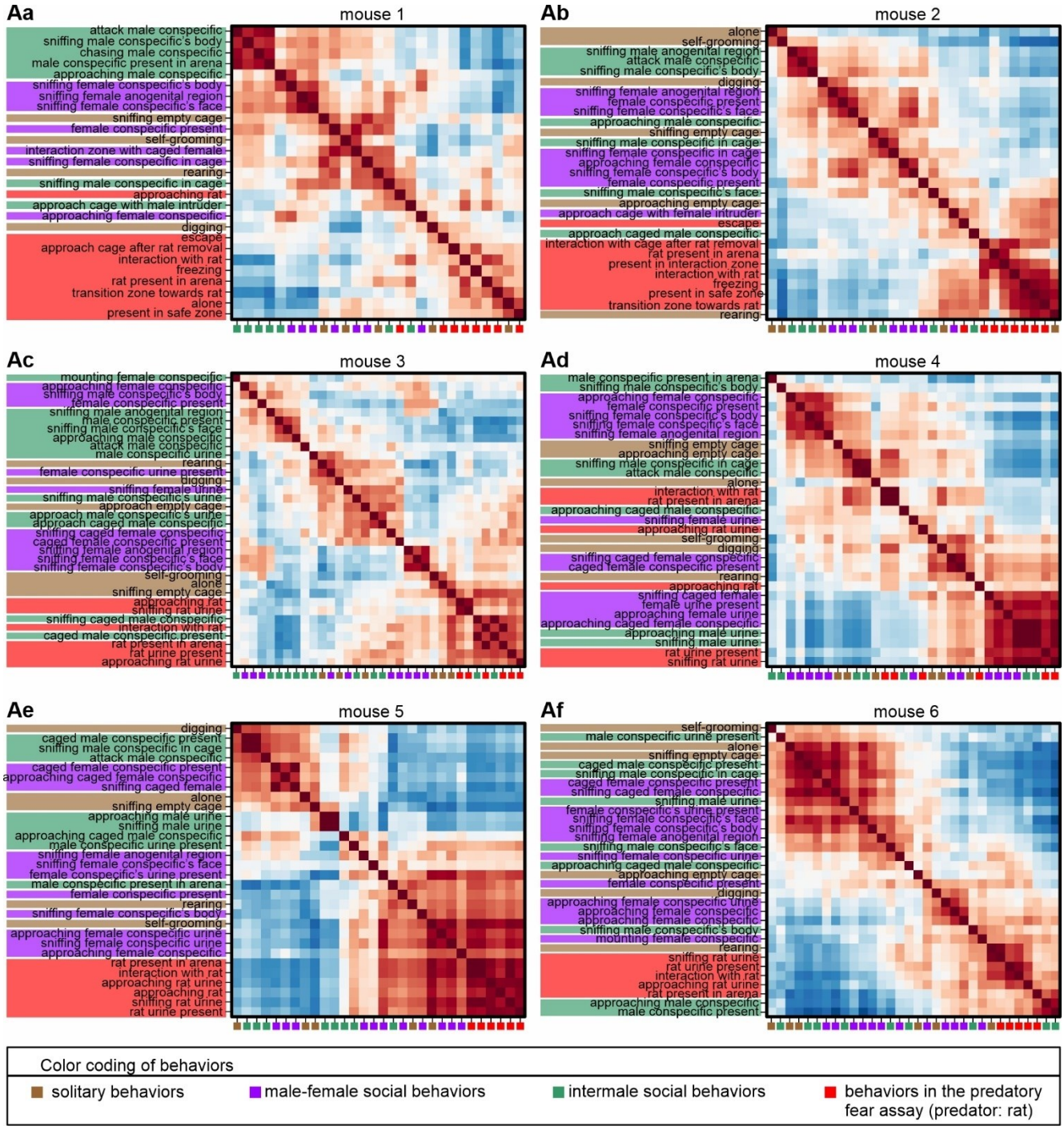

Figure S3. Correlation matrix of behavior for each of the recorded six mice, related to Figure 3

(Aa-Af) Correlations matrices of behavior per mouse, rows (and columns) sorted based on similarity using the rastermap algorithm. Note the segregation of fear behavior actions (marked in red) towards the end of the row labels in each matrix (with the exception of mouse #4), while other behavior are intermingled.

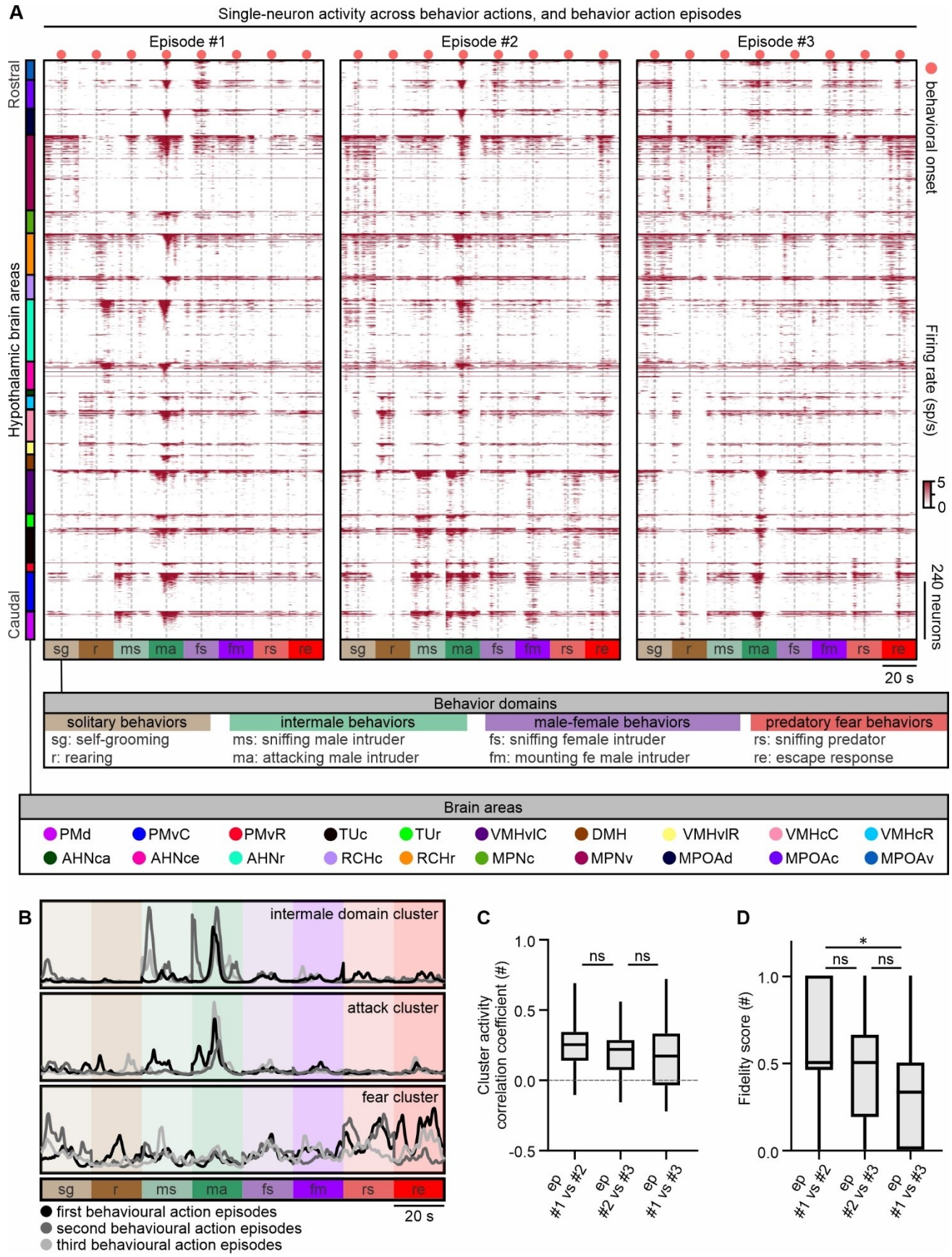
A
Single-neuron activity across behavior actions, and behavior action episodes
Episode #1
Episode #2
Episode #3
Rostral
Hypothalamic brain areas
Caudal
behavioral onset
Firing rate (sp/s)
5
0
240 neurons
sg r ms ma fs fm rs re
20 s
Behavior domains
solitary behaviors
sg: self-grooming
r: rearing
intermale behaviors
ms: sniffing male intruder
ma: attacking male intruder
male-female behaviors
fs: sniffing female intruder
fm: mounting fe male intruder
predatory fear behaviors
rs: sniffing predator
re: escape response
Brain areas
PMd PMvC PMvR TUc TUr VMHvlC DMH VMHvlR VMHcC VMHcR
AHNca AHNce AHNr RCHc RCHr MPNc MPNv MPOAd MPOAc MPOAv
B
intermale domain cluster
attack cluster
fear cluster
first behavioural action episodes
second behavioural action episodes
third behavioural action episodes
C
Cluster activity correlation coefficient (#)
1.0
0.5
0.0
-0.5
ns
ns
ep #1 vs #2
ep #2 vs #3
ep #1 vs #3
D
Fidelity score (#)
*
ns
ns
1.0
0.5
0.0
ep #1 vs #2
ep #2 vs #3
ep #1 vs #3

804

Figure S4. Single unit activity across four behavior domains, eight behaviors of interest, and three behavior episodes, related to Figure 4

(A) Single unit activity in eight behaviors of interest during three consecutive behavioral episodes/instances (n=6 mice, 2347 neurons).

(B) Selected clusters from panel A of Figure 4, indicating the activity of each cluster across the first, second and third behavioral action episodes.

(C) Correlation coefficient of average cluster activity across behavioral episodes (relevant to Figure 4A).

(D) Fidelity score of cluster identity across behavior episodes; a measure that quantifies the degree to which a cluster is active to the exact same behavior(s). A cluster considered active during the expression of any single behavior, scales its activity above the threshold of two standard deviations (as compared to its baseline activity).

ns: statistically not significant, $*P < 0.05$. Statistical comparisons of the data shown in panels (B, C) were performed through One-Way ANOVA and Dunnett's post-hoc test was used to correct for multiple comparisons. In box-and-whisker plots, center lines indicate medians, box edges represent the interquartile range, and whiskers extend to the minimal and maximal values.

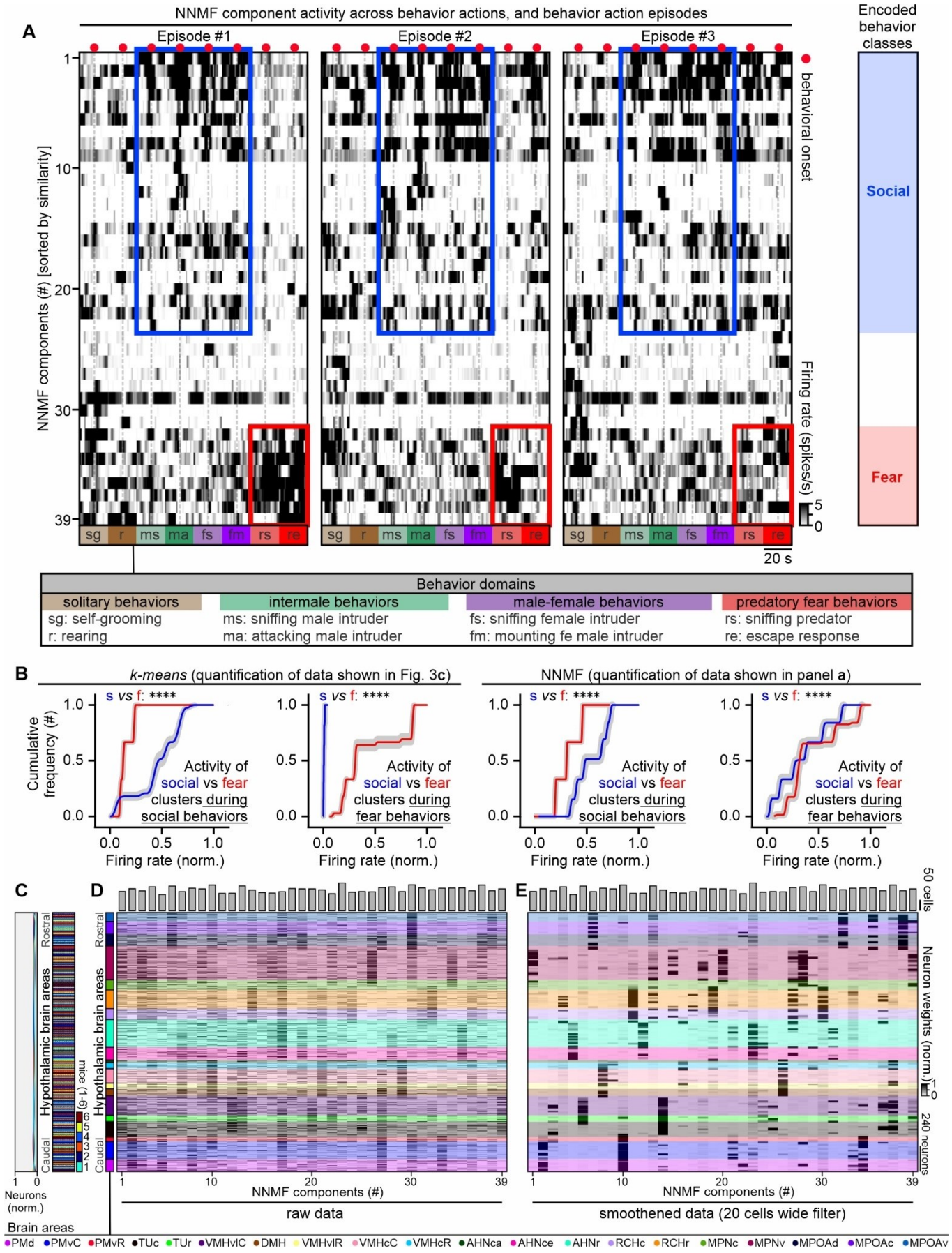
A
NNMF component activity across behavior actions, and behavior action episodes
Episode #1
Episode #2
Episode #3
Encoded behavior classes
behavioral onset
Social
Fear
NNMF components (#) [sorted by similarity]
Firing rate (spikes/s)
20 s
sg r ms ma fs fm rs re
Behavior domains
solitary behaviors
sg: self-grooming
r: rearing
intermale behaviors
ms: sniffing male intruder
ma: attacking male intruder
male-female behaviors
fs: sniffing female intruder
fm: mounting fe male intruder
predatory fear behaviors
rs: sniffing predator
re: escape response
B
k-means (quantification of data shown in Fig. 3c)
NNMF (quantification of data shown in panel a)
s vs f: ****
Cumulative frequency (#)
Activity of social vs fear clusters during social behaviors
Activity of social vs fear clusters during fear behaviors
Firing rate (norm.)
C
D
E
Rostral
Caudal
Hypothalamic brain areas
mice (1-6)
Neurons (norm.)
NNMF components (#)
raw data
smoothened data (20 cells wide filter)
50 cells
Neuron weights (norm.)
240 neurons
Brain areas
PMd PMvC PMvR TUc TUr VMHvlC DMH VMHvlR VMHcC VMHcR AHNca AHNce AHNr RCHc RCHr MPNc MPNv MPOAd MPOAc MPOAv

821 **Figure S5. Non-negative matrix factorization (NMF) identifies ensembles with behavior class**
822 **specificity and spatial bias, related to Figures 4 and 5**

823 (A) NMF matrix factorization of the single neuron activity data shown in Figure S8, generates 39 NMF
824 components (collectively explaining 79% of the variance of the single unit data, a number selected using
825 the elbow method). Activity of components occurs somewhat similarly to the *k*-means clusters identified
826 and shown in Figure 3, during the social and fear behavior classes.

827 (B) Cumulative frequency of recorded firing rates in "social" or "fear" clusters identified in the *k*-means
828 (Figure 4) and NMF (present figure) analysis respectively. Note that cluster activity is significantly different
829 between conditions, but magnitude of effect is smaller in the NMF analysis.

830 (C) Histogram (left) and raster plot (right) showing neuron origin from the six recorded mice.

831 (D) Neuron weights of the NMF components (raw data, n=6 mice).

832 (E) Neuron weights of the NMF components (smoothened data [Gaussian smoothing filter with twenty
833 cells size], n=6 mice).

834 ****$P < 0.0001$. Statistical comparisons were performed through the Kolmogorov-Smirnov test.
835 Abbreviations of brain areas presented in the legend of Figure 1.

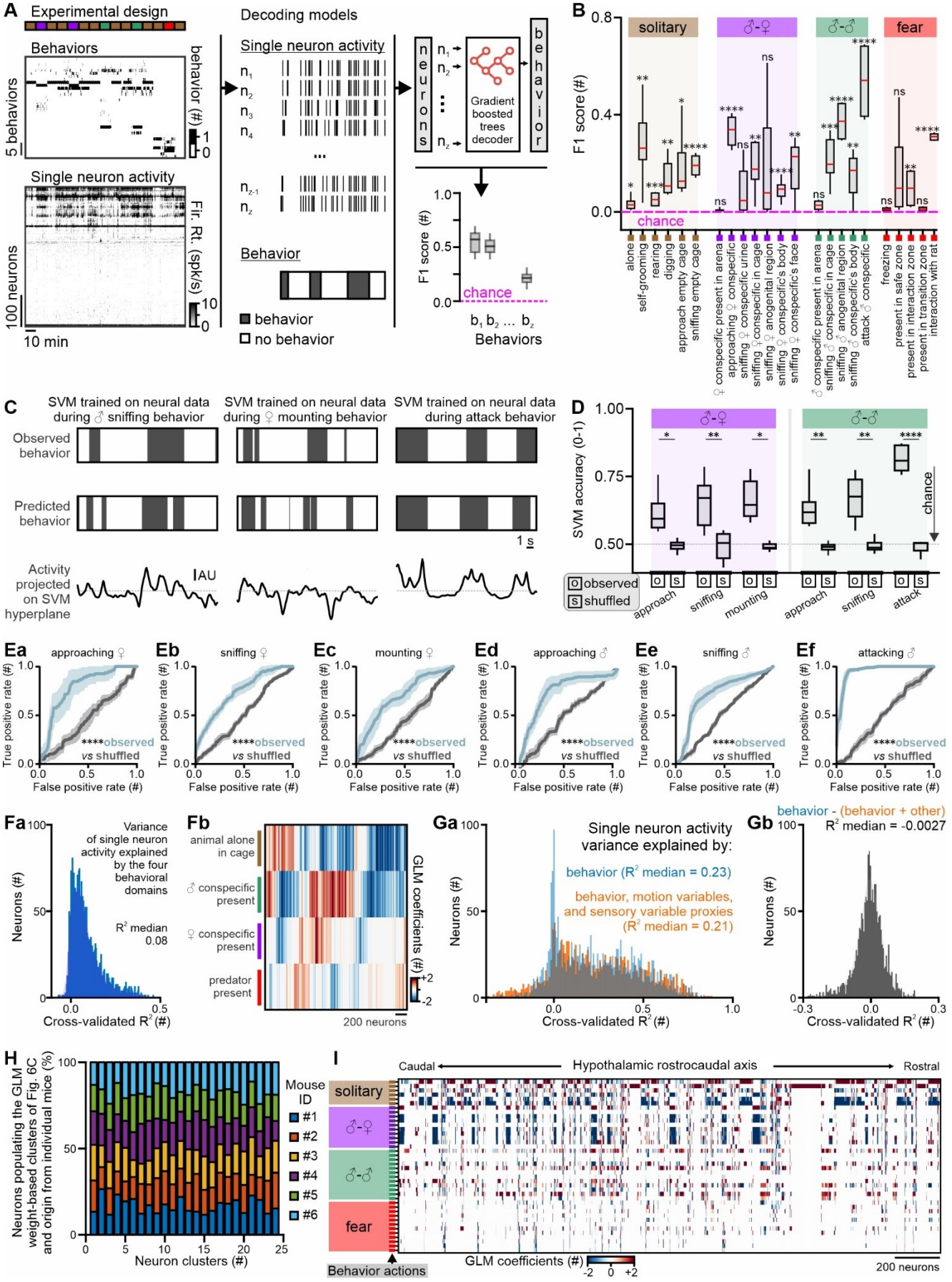
A
Experimental design
Behaviors
5 behaviors
behavior (#)
Single neuron activity
100 neurons
Fir. Rt. (spk/s)
10 min
Decoding models
Single neuron activity
Behavior
behavior
no behavior
neurons
Gradient boosted trees decoder
behavior
F1 score (#)
chance
Behaviors
B
solitary
♂-♀
♂-♂
fear
F1 score (#)
chance
alone
self-grooming
rearing
digging
approach empty cage
sniffing empty cage
conspecific present in arena
approaching ♀ conspecific
sniffing ♂ conspecific urine
sniffing ♀ conspecific in cage
sniffing ♀ anogenital region
sniffing ♀ conspecific's body
sniffing ♀ conspecific's face
conspecific present in arena
sniffing ♂ conspecific in cage
sniffing ♂ anogenital region
sniffing ♂ conspecific's body
attack ♂ conspecific
freezing
present in safe zone
present in interaction zone
present in transition zone
interaction with rat
C
SVM trained on neural data during ♂ sniffing behavior
SVM trained on neural data during ♀ mounting behavior
SVM trained on neural data during attack behavior
Observed behavior
Predicted behavior
Activity projected on SVM hyperplane
AU
1 s
D
SVM accuracy (0-1)
chance
observed
shuffled
approach
sniffing
mounting
approach
sniffing
attack
Ea approaching ♀
Eb sniffing ♀
Ec mounting ♀
Ed approaching ♂
Ee sniffing ♂
Ef attacking ♂
True positive rate (#)
False positive rate (#)
****observed vs shuffled
Fa
Variance of single neuron activity explained by the four behavioral domains
R² median 0.08
Neurons (#)
Cross-validated R² (#)
Fb
animal alone in cage
♂ conspecific present
♀ conspecific present
predator present
GLM coefficients (#)
200 neurons
Ga
Single neuron activity variance explained by:
behavior (R² median = 0.23)
behavior, motion variables, and sensory variable proxies (R² median = 0.21)
Neurons (#)
Cross-validated R² (#)
Gb
behavior - (behavior + other)
R² median = -0.0027
Neurons (#)
Cross-validated R² (#)
H
Neurons populating the GLM weight-based clusters of Fig. 6C and origin from individual mice (%)
Neuron clusters (#)
Mouse ID
#1
#2
#3
#4
#5
#6
I
Caudal
Hypothalamic rostrocaudal axis
Rostral
solitary
♂-♀
♂-♂
fear
Behavior actions
GLM coefficients (#)
200 neurons

Figure S6. Decoding behavior from single neuron activity, and encoding models explaining single neuron activity variance based on different predictor variables,related to Figure 6

(A) Schematic of the analysis pipeline using gradient-boosted trees for binary decoding of behavior based on single unit activity.

(B) Shuffled F1-score subtracted, k-fold cross-validated F1-score output of decoding behavior based on the gradient boosted trees decoders (box plots are made of points from the six recorded mice – each mouse contributing a single point unless a behavior was not expressed by an individual). In box-and-whisker plots, center lines indicate medians, box edges represent the interquartile range, and whiskers extend to the minimal and maximal values.

(C) Example accuracy of three decoders on the test data of three social behaviors, and activity projected on the SVM hyperplane.

(D) Decoder accuracy on social behaviors of interest (n = 6 mice).

(Ea-Ef) ROC curves on the observed and shuffled data of specific social behaviors (n = 6 mice).

(Fa) Variance explained (cross-validated, shuffled data R^2 subtracted, R^2) of single-neuron activity (n=6 mice, 2347 neurons) based on the four behavioral domains of interest, solitary, male intruder in arena, female intruder in arena, and predator in arena. Output of Poisson-GLM.

(Fb) Behavioral domain coefficients on single neurons recorded across all mice (n=6 mice).

(Ga) Overlap of two histograms of cross-validated R^2 values generated by GLMs. Light blue: Variance explained (cross-validated, shuffled data R^2 subtracted, R^2) of single-neuron activity (n=6 mice, 2347 neurons) based on forty annotated behaviors. Orange: Variance explained (cross-validated, shuffled data R^2 subtracted, R^2) of single-neuron activity (n=6 mice, 2347 neurons) based on forty instinctual behaviors, two motion-related variables, i.e., animal's velocity, animal's acceleration, and two sensory proxy variables, i.e., distance and angle between animals.

(Gb) Difference in the variance explained by behavior vs. behavior + motion-related and sensory proxy variables. Histogram was generated by subtraction of each neuron's R^2 generated via GLMs trained and tested only using annotated behaviors as predictor variables, against the neuron's R^2 generated via

863 GLMs trained and tested using annotated behaviors and motion variables as predictors. The peak around
864 R^2=0 is suggestive that motion variables explain little if any of the variance of hypothalamic single neuron
865 activity.
866 (H) Neuron contribution from each of the recorded mice to the neural branches presented in Figure 6C.
867 (I) Sorting neurons based on their spatial coordinates (as compared to the agglomerative linkage
868 clustering-based sorting using behavior coefficients shown in Figure 6C).
869 ns: statistically not significant, *P < 0.05, **P < 0.01, ***P < 0.001, ****P < 0.0001. In box-and-whisker
870 plots, center lines indicate medians, box edges represent the interquartile range, and whiskers extend to
871 the minimal and maximal values.

872 **STAR★METHODS**

873 **Experimental animals**

874 All experiments involving the use of living animals or their tissues adhered strictly to the guidelines set
875 by the National Institutes of Health (NIH). They were conducted under the approval of both the
876 Institutional Animal Care and Use Committee and the Institutional Biosafety Committee at the California
877 Institute of Technology (Caltech). Swiss Webster (CFW) mice (Crl: CFW [SW]), C56BL/6NCrl mice, and
878 Long-Evans (Crl:LE) rats were purchased from Charles River US. In all behavioral and resident-intruder
879 assays, wild-type mice from the C56BL/6NCrl strain were used (sourced from Charles River
880 Laboratories). Experimental animals were provided with additional enrichment and running wheels in
881 their cages, were maintained in good health, and were monitored by the local veterinarian. Housing
882 conditions for the mice were carefully monitored. Ventilated micro-isolator cages were maintained in an
883 environment with stable temperature (23°C) and humidity (55-60%). A reverse light-dark cycle of 12 hours
884 each was used, and animals were provided unlimited access to food and water. The cages were cleaned
885 and changed once a week on a specific day, and no experiments were conducted within two days of a
886 cage change.

887

888 **Selection of animals for experiments**

889 *In vivo* electrophysiology data were collected from six Swiss-Webster mice (out of 11 implanted animals
890 generated in a single cohort) and are reported here. Mice were selected for combined electrophysiology
891 and behavior experiments based on the following criteria: (1) recovered within two days to pre-
892 implantation baseline behaviors, (2) expressed the majority of instinctual behaviors on the experimental
893 days, and (3) identified single neurons did not show drift across experimental sessions.

894

895 **Surgical methods**

896 All surgical and behavioral procedures adhered to the standards set by the National Institutes of Health
897 and received approval from the Institutional Animal Care and Use Committee at Caltech. Male Swiss

898 Webster mice, aged between 3-4 months, were used for neural recordings during behavior. Male mice
899 were used to avoid potential confounding effects of the estrous cycle in female mice.
900 Prior to surgery, mice were provided with medicated food cups (MediGel CPF, Clear H20 74-05-5022),
901 containing carprofen, for two days. Throughout the surgical procedure, mice were kept anesthetized with
902 isoflurane. The initial steps included removing the skin and clearing any underlying connective tissue.
903 The tissue surrounding the skull edges was securely adhered with Vetbond (Santa Cruz Biotechnology,
904 cat. no. sc-361931), and the skull surface was prepared by being scraped, dried, and textured.
905 A custom boomerang-shaped titanium head bar was affixed to the occipital bone of the skull, and a hole
906 for the ground screw was carefully drilled, placing the screw above the right prefrontal cortex. Optibond
907 Solo Plus (Kerr, cat No. 31514) was applied to the skull and cured under UV light. Charisma (Net32, cat.
908 No. 66000085) was employed to establish a base for the implant and to reinforce the area around the
909 ground screw.
910 With the help of a dental drill, eight 100 μm holes were made above the somatosensory cortex. These
911 holes were designed to accommodate the eight shanks of the silicon probe, aimed at penetrating the
912 deep brain. The entire silicon probe assembly, including the probe and headstage, was placed in the
913 stereotax. Post-application of DiD' (ThermoFisher Scientific, cat. no. D7757) on the posterior to the
914 electrode surface of each shank, the probe was gently lowered into the brain at a speed of 6 μm/sec
915 resulting in an insertion time of fifteen minutes. Higher insertion speeds negatively impacted post-surgery
916 recovery and neuron yield per mouse.
917 The precise coordinates for probe insertion and the angle of attack were adapted for each mouse
918 accommodating idiosyncratic differences in cortical vasculature identified post-drilling, and enabling the
919 recording of the same deep brain structures. The ground wire was soldered to the ground screw and
920 Metabond cement was used to secure the probe and headstage to the skull. The entire assembly was
921 wrapped in Kapton Tape (ULINE S-7595), followed by a recovery period typically extending to two weeks.
922 Post-surgery, mice were individually housed, and additional enrichment elements were provided. Daily
923 monitoring was performed to evaluate locomotion and the expression of behaviors (self-grooming, rearing

924 and digging). Between the second and third weeks, mice were acclimatized in test arenas to examine
925 their natural movement and the manifestation of thigmotaxis in the open field test, among other behaviors.
926

927 **Behavioral tests**

928 All behavioral tests were performed during the dark phase and under dim red light between 2 h after the
929 initiation of the dark phase and three hours before the initiation of the light phase. Mice were acclimated
930 to the testing behavior room for a minimum of one hour before testing with *ad libitum* access to food and
931 water. Videos were recorded using the GS3-U3-51S5C-C 2/3" FLIR Grasshopper®3 USB 3.0 Color
932 Camera, at thirty frames per second. Video acquisition was triggered through a TTL signal provided to
933 the *trigger*-in GPIO port of the camera, by the neural data acquisition software Allego – NeuroNexus'
934 proprietary software for data acquisition. Timestamps for frames were collected and recorded as an
935 auxiliary signal through the software Allego and NeuroNexus' data acquisition box (SmartBox Pro).
936

937 **Resident–intruder (RI) test**

938 The resident's cage was not cleaned for a minimum of 2 days before the behavioral test. A single male
939 or female intruder was introduced per testing session. A ten-minute habituation period was allowed and
940 recorded, and was followed by the introduction of a freely moving intruder for ten minutes or an intruder
941 within a perforated cage. Video and neural data acquisition continued for ten minutes following the
942 removal of the intruder. Intruders were of the C57BL/6N background, and were either intact males, or
943 intact females in the estrus phase of the estrous cycle (stage of cycle was defined by inspection of vaginal
944 smears, and the cycle of individual female intruders was followed for three consecutive days prior to the
945 day of the experiment). Behaviors during the RI test were video recorded using a top view camera, and
946 were manually annotated using BENTO[70] (https://github.com/neuroethology/bentoMAT).
947
948
949

950 **Predatory fear (PF) behavioral assay**

951 A custom four-chamber arena was used to present a caged-predator. All but the front sides of the cage
952 of the predator were opaque white colored, with the exception of the front side that was clear and the
953 wall was perforated evenly with square holes five square millimetres in size placed fifteen millimetres
954 apart (center to center). This design aims to allow diffusion of pheromonal cues that may affect the
955 behavior of pray animals. Other than the chamber containing the predator, the arena includes three other
956 chambers: i) the interaction zone chamber that allows the mouse to sniff the predator and interact with
957 the cage before, during and after the presence of the rat in the arena. ii) The transition zone chamber
958 that allows the mouse to move between the proximal and furthest away chambers from the rat, and iii)
959 the safe zone chamber, that places a large distance between the mouse and the predator. The validation
960 parameters of this custom experimental design are presented in extended data figure four.

961

962 **Behavior annotations and quantification of behavior**

963 Behavior videos were manually annotated using BENTO[70] (freely available software package:
964 https://github.com/neuroethology/bentoMAT). A total of forty-three behaviors during the resident intruder
965 and predatory fear assays were annotated. The behavioral videos were loaded into MATLAB, and a
966 trained individual blind to the experimental design annotated the videos frame-by-frame for all behavior
967 actions. Behavior annotations were then further edited by an expert (author: S.S.) who was not blind to
968 the experiment conditions. Imaging frames were spatially downsampled by a factor of two, a modification
969 that we recognize to not influence the identification of the behaviors of interest and that facilitates
970 smoother processing of the videos by BENTO[70] in MATLAB. Behavior features including velocity,
971 acceleration, distance, and angle between animals were calculate using DeepLabCut[38], and custom
972 MATLAB routines.

973

974 ***In vivo* electrophysiology**

975 *In vivo* electrophysiology recordings were performed in freely moving mice, using chronic silicon probe
976 implants. All extracellular recordings were conducted across the rostrocaudal hypothalamic axis of the
977 left hemisphere. Recordings were performed using a 256-channel custom-built for this specific project
978 silicon probe, the A8x32-Poly2-7.5mm-25s-325-177 NeuroNexus probe, now commercially available.
979 This specific probe includes eight shanks evenly spaced by 325 μm, and each shank at its lower end
980 contains two columns of electrodes, each electrode with a 25 μm distance from the next. The recording
981 area of each electrode was designed to be 25 μm^2. The length of each shank was 7.5 mm to enable the
982 probe to reach the model ventral nuclei of the deep brain in the hypothalamus.
983 Electrophysiology data was collected with Allego (proprietary software of NeuroNexus, recently updated
984 to Radiens [https://www.neuronexus.com/products/software/radiens/]), at 20 kHz sampling frequency.
985 Kilosort 2.5 was used for spike sorting [30], and we refined its output with manual curation of the results
986 through phy: https://github.com/kwikteam/phy. Neurons that exhibited drift or units that had multiunit
987 activity were excluded. To assess the neural recordings and perform basic related analysis prior to
988 exploring the data relevant to behavior, we used MATLAB code that can be found here:
989 https://github.com/cortex-lab/spikes. The quality of recordings was assessed through quantification of the
990 event rate, i.e., the frequency of spikes that are higher than the background noise level. We considered
991 an 'event' to be any occurrence that matches in time (less than one millisecond) and space (50 millimeters
992 in radius) and that has a strength that is at least six times greater than the median absolute deviation
993 (MAD) [71]. Secondly, for unit quality assessment, we computed and plotted the signal-to-noise ratio (SNR)
994 for each event. Event detection (spikes), spike amplitudes, and firing rates were further inspected with
995 custom MATLAB routines (https://github.com/jenniferColonell/Neuropixels_evaluation_tools).
996

997 **Whole-brain Imaging and Anatomical Registration of Probe Electrodes**

998 Brains that had been cleared, were imaged using the LaVision BioTec UltraMicroscope II in dibenzylether
999 at two different wavelengths: 488 nm (which creates green autofluorescence) and 632 nm (which allows
1000 for the visualization of electrode tracks through the DiD dye, a fixable, lipophilic far-red dye that remains

1001 stable even in dehydrated conditions). The imaging was done using an Olympus MVPLAPO 2X/0.5
1002 objective, a 5 μm step size, approximately 5 μm pixel size (at 0.8X magnification), and a single light sheet
1003 focus. The imaging only included the hemisphere of the brain where the electrode tracks were located,
1004 and it was carried out in a sagittal orientation.
1005 Images obtained from the green and far-red channels were subsequently downsampled to a 25 μm
1006 resolution by means of averaging. The green channel was then matched to the Allen Brain Atlas CCFv3
1007 autofluorescence atlas with a 25 μm resolution using a two-step process: an initial affine transformation
1008 followed by a nonlinear transformation carried out in Elastix. Previous studies have demonstrated that
1009 this method has an average registration error of about four voxels (or 100 μm). The same transformation
1010 process was also applied to the red channel.
1011 Electrode tracks were traced in the registered space using a custom R code that is based on AllenCCF
1012 (https://github.com/cortex-lab/allenCCF). This was done after electrophysiological recordings were made
1013 following the placement of a chronic implant that targeted the full anterior-posterior length of the
1014 hypothalamus.
1015 For the final analysis, brain regions were organized into twenty distinct groups based on the Allen Brain
1016 Atlas hierarchy. The specific location of each unit was determined based on where that unit produced the
1017 highest amplitude on the electrode. The location along each electrode was transformed into the Allen
1018 Brain Atlas space according to the orientation and position of the traced electrode track for each
1019 recording. The final part of allocating each electrode to a hypothalamic region was performed manually,
1020 to further improve the output of the earlier-mentioned process. For each mouse, a unique spatial map of
1021 electrodes/hypothalamic brain areas was defined and was later used to assign individual extracellular
1022 units to specific anatomical regions.
1023

1024 ***k*-means clustering**

1025 The variance explained by a clustering solution in the context of the *k*-means algorithm reflects the
1026 proportion of the total variance in the dataset that is "captured" by the centroids of the clusters. In other

words, it indicates how well the centroids represent the data. For computing the variance explained is we used the sum of squared distances between data points and their assigned cluster centroids. The more the variance explained, the closer the data points are to their respective centroids, and hence the better the clustering solution. Specifically, we calculated within-cluster sum of squares (WCSS). After performing *k*-means clustering we obtained the cell indices, which provide the cluster assignments for each data point, and the centroids for the clusters. The sum of squared distances of each point to its cluster centroid gives us the WCSS. We then iterated over all data point. For each point, we calculated the squared Euclidean distance between the point and its assigned centroid and summed these squared distances. We then computed the total sum of squares (TSS). i.e., the sum of squared distances of each point from the overall mean of the data. The variance explained by the clustering solution can be found by subtracting the WCSS from the TSS and then dividing by the TSS. Note that as the number of clusters *k* increases, the WCSS tends to decrease (each point can be closer to its centroid), but there's usually a diminishing return. This is often visualized with an "elbow plot," where the rate of decrease in WCSS slows down after a certain number of clusters, indicating a potential good choice for k.

GLM output – functional vs. spatial distribution of clusters

Neuronal cluster data was analyzed to determine its relationship with four predefined behavioral categories. For each cluster, its activity was averaged across specific row ranges corresponding to each category. Negative activity was disregarded, and data was normalized using the z-score to mitigate outlier effects. The entropy was computed for each cluster based on its normalized activity distribution across behavioral categories. Entropy was utilized to quantify the distribution of each neuronal cluster's activity across the four behavioral categories. After averaging the activity for each category and normalizing these averages to form a probability distribution, the entropy was computed using the formula for a discrete probability distribution. This measure provided insights into whether a cluster's activity predominantly aligned with specific behavioral categories (low entropy) or was distributed across multiple categories (high entropy). For spatial analysis, a "center of mass" approach was employed to gauge the

distribution of each cluster's activity across 20 assumed brain regions. Both the functional (behavioral category-based) and spatial distributed-ness of each cluster were then visualized using a scatter plot.

Decoding Analysis

Gradient boosted trees: neuronal data (spike rates, binned at 100 ms) was smoothened through convolution with a Gaussian kernel of 10 timesteps (1 second). The data to the decoder was then made recurrent by creating a temporal window of size ten at each given timestamp. The data was then flattened before decoding. The data was analyzed using five-fold cross-validation. Each behavior was decoded individually based on the activity of all neurons. Folds were created by determining the onsets of the behavior and then creating a temporal window of the length of the behavior before its onset. All events were concatenated, and cross-validation was performed on the resulting data. The decoding was performed using gradient-boosted trees [72,73] (depth of 3, 50 estimators, lr = 0.01). Performance was evaluated by calculating the cross validated, shuffled data subtracted F1-score per behavior. For each behavior, we calculated the maximum performance within a specific temporal jitter (10 timesteps). We then averaged performances across animals.

Support Vector Machines: To assess if single-neuron activity holds information about specific social actions, we trained a unique binary linear decoder for each behavioral action to predict whether or not the behavior was taking place. To ensure the behavior's representations weren't mixed with the representations of the intruder's gender, we created separate decoders for behaviors directed towards males and females. When the behavior of interest was not being exhibited, we under-sampled the negative training data to balance the number of positive and negative training examples. We then used these binary labels alongside their matching activity vectors to train a linear SVM decoder.

Code Availability

The code used for analysis in this study is available upon request from the first author (stefanos.stagkourakis@gmail.com).